Identifying Electrochemical Processes by Distribution of Relaxation Times in Proton Exchange Membrane Electrolyzers

Ai-Lin Chan[a], Haoran Yu[b], Kimberly S. Reeves[b], Shaun M. Alia[a,*]

[a] Chemical and Material Sciences Center, National Renewable Energy Laboratory, 15013 Denver West Parkway, Golden, 80401, Colorado, United States
[b] Center for Nanophase Materials Sciences, Oak Ridge National Laboratory, 1 Bethel Valley Rd, Oak Ridge, 37830, Tennessee United States

Abstract

Distribution of relaxation time (DRT) is used to interpret electrochemical impedance spectroscopy (EIS) for proton exchange membrane (PEM) water electrolyzers, with an attempt to separate overlapped relaxation processes in Nyquist plots. By varying operating conditions and catalyst loadings, four main relaxation peaks arising from EIS can be identified and successfully separated from low to high frequencies as (P1) mass transport, (P2) oxygen evolution reaction kinetics, (P3) reaction kinetics (with faster time constant than P2), and (P4) ionic transport. The shape, height, and frequency of the DRT peaks change with different membrane electrode assembly (MEA) configurations. Electron microscopy reveals distinct features from the cross-sectioned MEAs which verify critical DRT results in that increasing the iridium (Ir)-anode loading from 0.2 mg_{Ir}/cm^2 to 1.5 mg_{Ir}/cm^2 reduces kinetic losses due to higher site-access; a thick and compacted anode, however, also triggers higher ohmic resistances from membrane/catalyst layer hydration and increases transport losses due to longer ionomer pathways. DRT provides higher resolution to EIS for deconvoluting processes with different relaxation times and the quantification of DRT peaks improves the accounting of total losses from each process.

Keywords: electrochemical impedance spectroscopy (EIS), distribution of relaxation times (DRT), modeling, proton exchange membrane (PEM) electrolysis

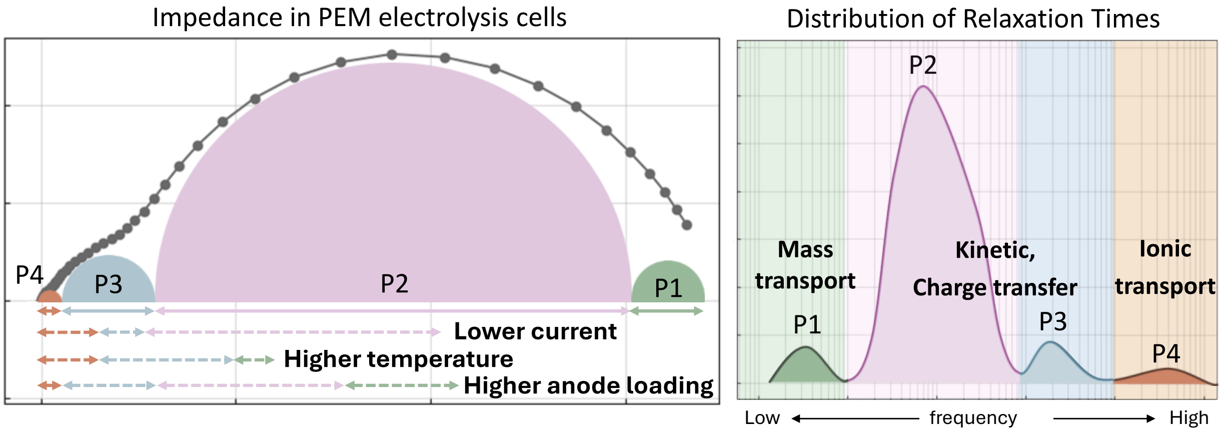

Highlights:

- **Ionic transport-related processes can be separated and quantified by DRT.**
- **Four relaxation processes were presented by varying currents and temperatures.**
- **The charge transfer processes were faster with higher Ir content at the anode.**
- **Lower cathode loading impacted on the main relaxation process (P2).**

1. Introduction

Hydrogen production via electrolysis has drawn more attention to provide flexibility for low cost intermittent power sources through storage and distribution, and provides value in being able to convert between electricity and chemical bonds. Among water splitting technologies, proton exchange membrane (PEM) electrolysis has the advantages of high efficiency and durability as well as the ability to reduce compression cost through backpressure with comparatively little hydrogen crossover[1–4]. To accelerate the commercial development of this technology, research efforts in PEM electrolysis typically focuses on aspects of cost reduction, performance enhancement, and lifetime extension[1,2]. Identifying voltage loss contributors and understanding electrochemical mechanisms during operation are necessary for optimizing efficiency and mitigating degradation, which creates tremendous interest in advanced electrochemical diagnostic methods.

Electrochemical impedance spectroscopy (EIS) is a widely used, nondestructive and noninvasive diagnostic method in electrochemical systems. Impedance interpretation can usually be done by evaluating Nyquist and Bode plots, such as resistive-capacitive and resistive-inductive features, Warburg impedances and the number of physical processes. However, processes with similar time constants (τ) merge into a single semi-circle in Nyquist plots and are difficult to separate. While EIS data can also be analyzed by equivalent circuit models (ECMs) for electrochemical properties, appropriate circuit elements and model configuration must be determined with a certain degree of familiarity to the systems to avoid overinterpretation[5]. Defining ECMs and assigning each time constant to a correlated polarization process during electrolysis can become complicated and challenging. In contrast, distribution of relaxation times (DRT) is a powerful method in identifying the number of time constants in a electrochemical system and in separating physical processes by their characteristic frequency without pre-assumption and prior knowledge[5–7]. This technique has been applied to fuel cells[6,8–11], lithium-ion batteries[12] and double layer capacitors since 1907 by Schweidler[12]. As in eqn (1), DRT applies a distribution gamma function $\gamma(\tau)$ into frequency-based EIS measurement, where j is the imaginary unit and ω is the angular frequency. R_{ohm} and R_{pol} is the ohmic resistance in the high frequency region of EIS and the diameter of semi-circle (polarization resistance) in Nyquist plot, respectively.

$$Z(\omega) = R_{ohm} + R_{pol} \int_0^{\infty} \frac{\gamma(\tau) d\tau}{1 + j\omega\tau} \tag{1}$$

In PEM fuel cells, losses related to reaction kinetics, proton/electron transport, and gas diffusion processes can be separated by DRT. Diffusion resistances in fuel cells caused by cathode flooding are further discussed by varying experiments design (relative humidity, temperature, reactant compositions) and are deconvoluted by differentalgorithms[6,9,13,14]. In PEM electrolysis cells (PEMECs), kinetic losses from the anode are elaborated by in and ex situ characterization methods because the anodic reaction involves several steps of electron transfer with similar reaction rates that are difficult to isolate with basic electrochemical experiments[15–21]. Combining

EIS and DRT for PEMEC is promising to deconvolute polarization processes. Li et al. first evaluated PEMECs with DRT in 2023[22], however, the electrochemical processes vary with different operating conditions and hardware/material. Different methodologies converting impedance data from a frequency to a time domain further affect the characteristic time constants of each process. The explanation of loss mechanisms and the evaluation of peak features (location, shape and overlapping) in a DRT result have also not been presented for PEMECs.

In this work, DRT is employed as the main impedance deconvolution method to elucidate different electrochemical processes during PEMECs operation. Implementing ECM and voltage break-down analysis can help verify the involved polarization processes and build the correlation to the DRT results. In PEMECs, since the oxygen evolution reaction (OER) at the anode is the largest contributor to overpotential in polarization curve[21,23], we will mainly focus on anodic processes. The results show that different Ir loadings (0.2 to 1.5 mg_{Ir}/cm^2) at the anode generated distinct DRT peaks features. Overall, by varying operating conditions (temperature and current) and tuning catalyst loadings, four main polarization processes can be identified and quantified in the DRT results, which leverage EIS interpretation for electrochemical mechanisms understandings and cell performance limitations in PEMECs.

2. Material and methods

2.1. Membrane electrode assembly (MEA) fabrication

MEAs were fabricated as catalyst-coated membranes (CCMs). Catalysts at the anode and cathode were unsupported Ir oxide (Alfa Aesar, 43396) and carbon supported Pt (Tanaka Kikinzoku Kogyo, TEC10E50E), respectively. To prepare the electrode ink, catalyst was mixed with water and n-propyl alcohol (ratio: 1.3 : 1.0) and sonicated in an ice bath for 5 min. Ionomer (Nafion DE2020) was then added into the ink to 20% (mass of solids) and sonicated 30 s by horn, 20 min by bath and 30 s by horn. The ink was coated on Nafion 115 on a vacuum plate at 80°C to form the catalyst layer at an ultrasonic spray station. Catalyst loadings were analyzed by X-ray fluorescence spectrometer (Fisher XDV-SDD XRF) at three different spots on MEAs to get an average value of the catalyst loading. The MEA samples tested and analyzed in this study were summarized in **Table 1.** To reach the higher catalyst loading for the anode of MEA 1.5Ir 0.1Pt, the flow rate and the spray cycles were 0.3 ml/min and 16 cycles, respectively. For MEA 0.6Ir 0.1Pt, the Ir content in the anode ink was 3 times more than for MEA 0.2 0.1Pt and the spraying setup is the same as for MEA 0.2Ir 0.1Pt.

Before cell assembly, MEAs were soaked in deionized water for 15 min. MEA was sandwiched between Pt-coated titanium porous transport layer (PTL from Giner Inc) at the anode and carbon gas diffusion layer (GDL from Fuel Cell Technologies) at the cathode. Aluminum end plates (Fuel Cell Technologies) were used to provide uniform pressure distribution and mechanical stability.

Table 1. The ink fabrication parameters of different MEAs. An and Ca is anode and cathode, respectively.

MEA (An/Ca)	An loading (mg_{Ir}/cm^2)	Ca loading (mg_{Pt}/cm^2)	Flow rate of spray (ml/min, An/Ca)	Cycles of spray (An/Ca)
0.2Ir 0.1Pt	0.2	0.1	0.2/0.2	36/32
0.6Ir 0.1Pt	0.6	0.1	0.2/0.2	36/32
1.5Ir 0.1Pt	1.5	0.1	0.3/0.2	64/32
0.2Ir 0.035Pt	0.2	0.035	0.2/0.2	36/16

All MEAs were activated by a conditioning protocol (0.2 A/cm^2 for 1 hour, 1 A/cm^2 for 1 hour, 2 V for 30 minutes, 1.7 V for 2 hours and 2 V for 30 minutes) at 80˚C[24]. During testing, water flow rate was controlled to 50 and 0 ml/min at the anode and cathode, respectively. After conditioning, repeated polarization curves were applied with a range of current densities, from 0.02 A/cm^2 to 4 A/cm^2 (anodic) and followed by a cathodic scan, for 20 days. Each current density was held for 5 min and the reported potential was the average within the last 10 sec of each step. At the end of life, an additional temperature study was conducted by electrochemical diagnostic at 3 different temperatures (40, 60 and 80˚C) for MEA 1.5Ir 0.1Pt.

2.2. Electrochemical methods

Galvanostatic impedance measurements were taken from 40k to 0.1 Hz with a 5% amplitude of the applied current, 10 points of frequency per decade by a potentiostat (Autolab PGSTAT302N) and a booster (20A). The Wave form is set as sinusoidal. For voltage breakdown analysis, EIS was measured at the currents corresponding to the current densities from 0.02 A/cm^2 to 0.8 A/cm^2 in polarization curves. Immediately after applying 1.6 V for 4 min, non-faradaic impedance (NFI) was analyzed by applying 1.25 V with the frequency range 100k - 0.1 Hz to obtain the catalyst layer (CL) resistance (CLR). We adopted linear fitting for CLR approximation, which was verified to show similar results with transmission line models in the previous study for PEMECs[17]. Cyclic voltammetry (CV) was measured from 0 V to 1.4 V with the scan rate of 20 mV/s immediately after 1 min of 2 V applied.

2.3. Impedance data processing and modeling

Since impedance modeling and DRT results were sensitive to non-linear impedance behaviors, the impedance configurations were optimized to avoid wiring artifacts and the data was checked via Kramer-Kronig (KK) test by impedance.py[25]. For the EIS presented in this work, the residuals of real and imaginary impedance from KK test were in the range of ±1% (**Figure S 1-S 3.**), which indicated the impedance responses followed KK relations[26]. After KK test, EIS were modeled by ECM with the circuit configuration showing in **Figure 1** (d). The circuit consisted of a modified inductance (L_a), an ohmic resistance (R_{ohm} or high frequency resistance, HFR), and four time constants in series. One time constant is a composite of a charge transfer resistance (R) in parallel to a constant phase element (CPE or Q). Modified inductance (L_a) was used, instead of pure inductance, to represent heterogeneity of inductive effects from the setup of cables and artifacts[27,28] and helped restore the features of impedance in the high frequency region, providing more precise evaluation of R_{ohm} and R1//Q1. The impedance generated by L_a is shown in eqn (2)[25,28], with a in the range 0 to 1, and a pure inductor when a=1. CPE was used to represent an inhomogeneous electrode surface and the CPE impedance is described by eqn (3)[13,28]. The equivalent capacitance from a CPE element is estimated as eqn (4), where ω_{max} is the frequency of the maximum imaginary impedance is[29]. The ECM results and the detailed descriptions were provided in section 3.1.1.

$$Z_{L_a} = L_a * (2\pi f)^a \tag{2}$$

$$Z_{CPE} = \frac{1}{Q(j2\pi f)^n} \tag{3}$$

$$C = Q(\omega_{max})^{n-1} \tag{4}$$

In this study, DRT results were obtained by using an open-source Python code developed in the publication[7]. Either real or imaginary part of impedance can be used to solve $\gamma(\tau)$ in eqn (1), as eqn (5) and (6) showed. For all the DRT results presented in this study, we used real part of impedance.

$$Z'(\omega) = R_{ohm} + R_{pol}\int_0^\infty \frac{\gamma(\tau)d\tau}{1 + j\omega^2\tau^2} \tag{5}$$

$$Z''(\omega) = -R_{pol}\int_0^\infty \frac{\omega\tau\gamma(\tau)d\tau}{1 + j\omega^2\tau^2} \tag{6}$$

However, eqn (5) and (6) are classified as the well-known ill-posed Fredholm integral equations of the first kind. The solution $\gamma(\tau)$ is close to Dirac delta function δ with a large gradient. To approximate a numerical solution of $\gamma(\tau)$, eqn (5) and (6) can be rewritten as eqn (7) and (8) based on the simplest numerical integration. Assuming a part of eqn (8) as a $m \times n$ matrix, it can be viewed as the expression of eqn (9), where $\vec{\gamma}$ and $\vec{Z}$" is the column vector with the length m and n, respectively. Same expression for real part of impedance can be formed from eqn (5).

$$Z'(\omega_m) = R_{pol} \sum_{n=1}^{N} \frac{\gamma_n \delta\tau_n}{1 + \omega_m^2 \tau_n^2} \tag{7}$$

$$Z''(\omega_m) = -R_{pol} \sum_{n=1}^{N} \frac{\omega_m \tau_n \gamma_n \delta\tau_n}{1 + \omega_m^2 \tau_n^2} \tag{8}$$

$$\vec{Z}" = A\,\vec{\gamma}, \qquad with\ A_{m,n} = -R_{pol} \frac{\omega_m \tau_n \delta\tau_n}{1 + \omega_m^2 \tau_n^2} \tag{9}$$

To solve the ill-posed problem, the DRT algorithms used in this study combined Tikhonov regularization (TR) and projected gradient (PG) iterations. Denoting the square of Euclidean norm, eqn (9) can be viewed as:

$$||Ax - b||^2 = 0, \qquad where\ ||A||^2 = A^T A \tag{10}$$

and A^T is the transposed matrix of matrix A. For TR method, the Tikhonov matrix includes in Tikhonov regularization parameter λ_T and identify matrix I to approximate the solution and to converge to the following minimization condition[10,11]. To solve eqn (11), the least-squares solution to a linear matric was used from a Python library (Scipy.linalg.lstsq) with trust region reflective (tfr) algorithm.

$$(A^T A + \lambda_T I)\vec{\gamma}^K - A^T \vec{Z}" \rightarrow\ min \tag{11}$$

TR method cannot ensure positive values of solution $\vec{\gamma}$ [7]. With PG iterations in eqn (12), the Tikhonov residual can be minimized by applying the condition $[\gamma = 0, if\ \gamma < 0]$. It iterated until the condition in eqn (11) was reached. For implementing the DRT analysis by this tool, the inputs of λ_T and λ_{pg} were required. The initial value λ_T was obtained by the L-curve method and λ_{pg} can be estimated by eqn (13) with the Frobenius norm (the subscript F). More detailed derivation of eqn (5) – (13) can be found in the literature[7].

$$\vec{\gamma}^{K+1} = \vec{\gamma}^K - \lambda_{pg}((A^T A + \lambda_T I)\vec{\gamma}^K - A^T \vec{Z}"), \qquad where\ k\ = 0, 1, \dots, K - 1 \tag{12}$$

$$\lambda_{pg} \cong \frac{1}{||A^T A + \lambda_T I||_F} \tag{13}$$

On the other hand, G-Function DRT method from the publication[7,14] was applied to obtain dimensionless DRT function G(τ). Eqn(1) can then be written as eqn (14) with the condition $G(\tau)$ = τ γ(τ). The DRT results were presented on a frequency scale ($G(f)$) to increase the visibility of peaks at low frequency range. The resistivity of each peak is calculated by the integral of peak area.

$$Z(\omega) = R_{ohm} + R_{pol} \int_{-\infty}^{\infty} \frac{G(\tau) dln(\tau)}{1 + j\omega\tau} \tag{14}$$

2.4. Electron Microscopy

Cross-sectional analysis of MEAs was performed using scanning transmission electron microscopy (STEM). MEAs were embedded in epoxy and then cut with diamond-knife ultramicrotomy targeting a specimen thickness of ~75 nm. High-angle annular dark field scanning transmission electron microscopy (HAADF-STEM) and energy-dispersive X-ray spectrum (EDS) images were recorded using a JEM-ARM200F “NEOARM” analytical electron microscope (JEOL Ltd.) operated at 200 kV, equipped with a dual windowless silicon-drift detectors (SDD) each with a 100 mm^2 active area, and a Talos F200X TEM (Thermo Fisher Scientific) operated at 200kV and dquiped with Super-X EDS system. EDS maps were processed using JEOL Analysis Station (JEOL Ltd.) and Velox (Thermo Fisher Scientific) with 4 pixel binning followed by applying a Gaussian filter. Anode cross-sections were also imaged using a scanning electron microscope (SEM) with a backscattered electron (BSE) detector on a Hitachi S4800 operated at 5 kV. The epoxy block that was used for microtome was re-polished and coated with carbon for SEM imaging. The thickness of the anode electrode was analyzed using a custom python code, averaging measurement of 4 images for each sample.

3. Results and Discussion

3.1. Data processing before DRT analysis

3.1.1. Processing high frequency impedance

The inductive behavior from impedance measurement needed to be removed prior to the DRT calculation[6,9]. In normal operation in PEM electrolysis, inductance in the high frequency region is attributed to instrument/wiring artifacts[27,30]. **Figure 1** (a) shows the DRT results with raw data, including the high frequency inductive region, resulted in a calculated impedance that did not follow the experiment data and the initial γ solution oscillated (around $\pm$ 400 s^{-1}) in **Figure S 4**. To obtain better fitting and a higher quality of DRT analysis, two approaches can be applied: (1)

cut-off approach (**Figure 1** (b)), by directly removing positive imaginary impedance; and (2) model-and-remove approach (**Figure 1** (c)), by applying an appropriate ECM to the EIS data and removing the impedance generated by the inductance in the circuit. With the model-and-remove approach, the DRT peak was smoother in the high frequency range (5 - 200 Hz), with less overregularization in the lower end frequency (0.1 - 0.3 Hz). At moderate current density and with MEAs that performed reasonably well, mass transport contributions were very small compared to kinetics. DRT in this way was consistent with voltage breakdown analysis, where the transport peak at low frequency was much less dominant than the kinetic contribution. Furthermore, Tikhovnov regularization and projected gradient iterations should give a minimum residual, which indicates the modeled impedance from DRT analysis is close to experimental values^7. The residuals from the regularization calculations in the model-and-remove approach (1.25e-04) and the cut-off approach (2.23e-04) were 2 orders of magnitudes less than DRT with the raw EIS data (4.80e-02) in **Table S 1.** Preprocessing of the impedance data affected the quality of DRT polarization peaks, and the DRT results presented in this work were therefore preprocessed by approach (2).

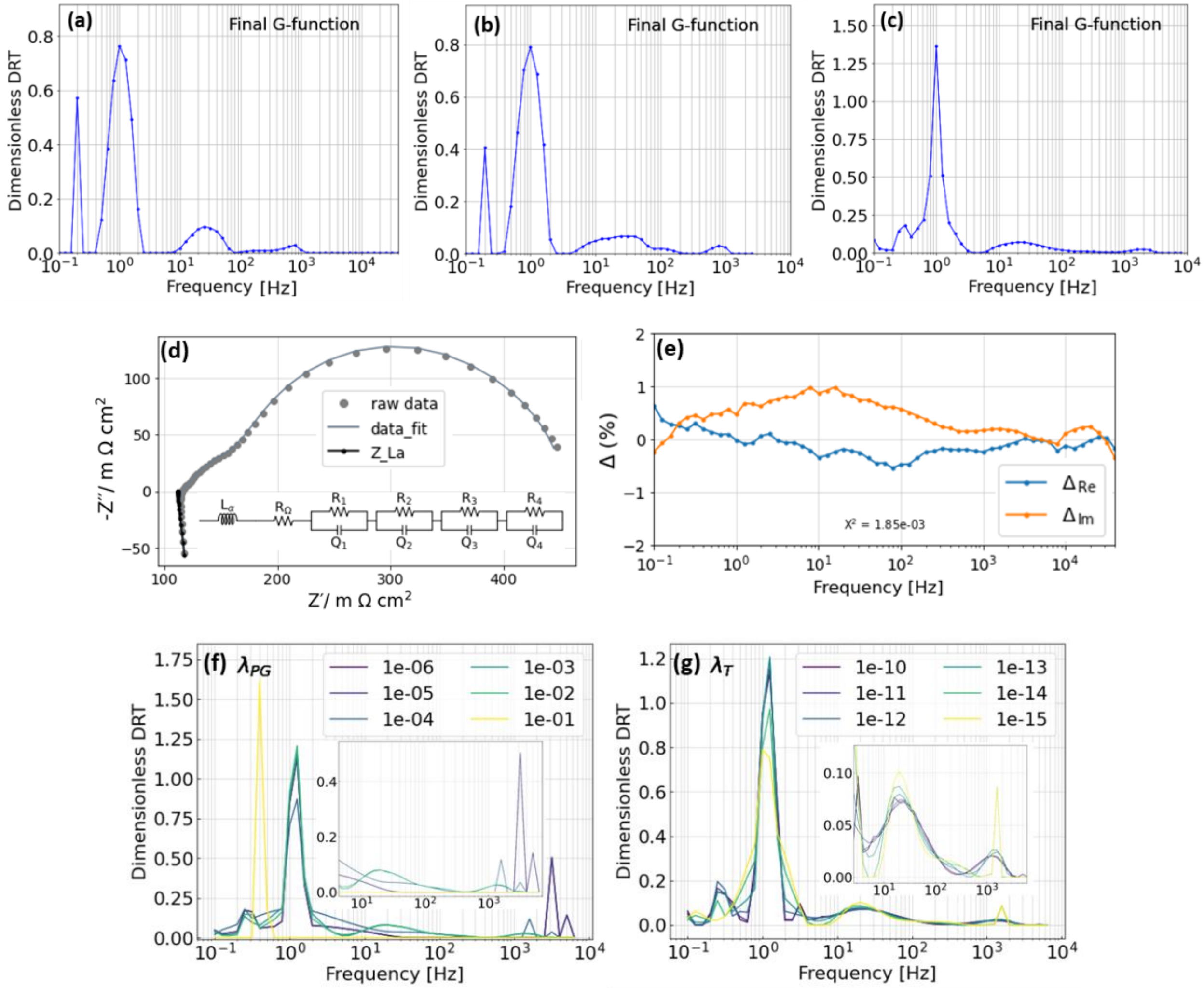

Figure 1. DRT analysis (a) with raw EIS data (b) by cut-off approach and (c) by model-and-remove approach. Regularization parameters are fixed ($\lambda_T = 10^{-13}$ and $\lambda_{pg} = 0.01$). EIS data was from 0.06 A/cm^2, 80°C with MEA 1.5Ir 0.1Pt. (d) ECM in (c). (e) Residuals of real and imaginary impedance from (d). (f) DRT results from varying the inputs of lambda parameters λ_{pg} and (g) λ_T

Although an optimal ECM for each different operational condition was not the focus of this study, a reasonable circuit configuration that fit the raw data was applied and shown in **Figure 1** (d) and (e) with real and imaginary impedance residuals within 1%. Assigning each time constant to a physical polarization process by ECM is not ideal because mathematical fitting process can generate multiple possibilities of different time constants. In this work, the purpose of ECM was to remove inductive effects from the measurements and to help reconstruct the data in high frequency area due to the severely distorted inductive region. The ECM results were provided in **Table S 2 – S 4**.

3.1.2. Selection of regularization parameters

Parameters in Tikhonov regularization and projected gradient iterations, λ_T and λ_{pg}, determine the characteristic frequencies, shapes and heights of DRT peaks[6,7]. Careful selection of the lambda inputs is needed to prevent over-regularization. In **Figure 1** (f), varying the λ_{pg} values from 10^{-6} to 10^{-1} gave a good example of overregularization and with $\lambda_{pg} = 10^{-6}$ to 10^{-4}, DRT results were not valid because of the extra oscillation around 10^3-10^4 Hz. With a larger λ_{pg} value ($\lambda_{pg} = 10^{-1}$), however, the features in middle-high frequency area were dismissed and the result gave a single spike between 10^{-1} and 1 Hz. The input of λ_{pg} values varying from 10^{-3} to 10^{-2} generated DRT results without overregularization for the high frequency range and gave information on peak features with less oscillation.

For λ_T, the DRT peaks did not show over-regularization effects with $\lambda_T = 10^{-11}$ - 10^{-13} in **Figure 1** (g). Below 10^{-13}, peaks with the frequency around 3 Hz contained a shoulder and generated larger DRT resistivity from the peak-area integration, which could have taken other polarization processes into account and was not preferred for differentiating between separate processes. λ_{PG} and λ_T were determined by the DRT results with the minimum Tikhonov residual (marked red in **Table S 5 – S 6**). For MEA 1.5Ir 0.1Pt, λ_{PG} and λ_T is 10^{-2} and 10^{-13}, respectively. In the next section, the process of assigning DRT peaks to possible polarization processes with different operating conditions and MEA configurations will be discussed.

3.2. Operating Conditions

3.2.1. Effect of current

For MEAs with higher anode loadings (MEA 1.5Ir 0.1Pt), **Figure 2** (a) shows a decreasing trend of polarization resistances at higher current due to more efficient charge transfer processes. The DRT results in **Figure 2** (b) further show distinct profiles at different current densities, and from 0.06 to 0.1 A/cm^2, 4 peaks were well discerned with different time constants. In **Figure 2** (c), the total polarization resistance decreased with increasing current density, for both DRT and ECM. The increasing HFR with current density was possibly due to lower water content in the membrane at high current, caused by more bubbles forming at the electrode interface and hindering water from reaching the membrane[13,19].

In **Figure 2** (b), P1 was located in the range of 0.15 - 3 Hz across all measured current densities and was associated with the lowest frequency impedance in **Figure 2** (a). P1 at 0.06 to 0.1 A/cm^2 had a sharper peak than at higher currents and had a resistivity of 10.83 to 19.43 mΩcm^2, possibly due to gas transport in the transport/catalyst layers and their interface.[14] For the current densities > 0.1 A/cm^2, the P1 resistivity was 1.78 to 2.32 mΩcm^2. The small contribution of P1 to the total impedance implied that P1 was related to mass transport, typically negligible in water electrolysis at low to moderate current density.

P2 was the dominant electrochemical process, and as shown in **Figure 2** (d), its peak frequency increased from 1.00 to 15.9 Hz and the resistivity decreased exponentially from 251.40 to 17.08 mΩcm^2 with increasing current density. A larger driving force enables access to a higher amount of active sites within the catalysts layer, and the triple phase boundaries are more distributed by electron flow at higher current densities[15,16]. The exponential relationship in **Figure 2** (d) implied that P2 can be attributed to kinetic losses based on the Tafel equation. Moreover, it indicated the number of active areas increased with current, yet gradually reached a threshold value when most of the available sites were active. When the current increased, P2 shifted toward a higher frequency range and was related to the decrease in charge transfer resistance (time constant $= R_{ct}*C = 1/(2\pi f)$). In ECM analysis, the time constant with a similar frequency range (0.99 to 16.4 Hz) accounted for a large portion of overpotential losses and aligned with the P2 resistivity in the DRT results. Moreover, voltage break down analysis verified that P2 is mainly from OER kinetic contributions. For the peak width, P2 was narrow and focused on a single peak frequency at low current densities (0.06 - 0.1 A/cm^2), which can be explained in that a smaller portion of catalyst layers take part at low current density and thus the polarization processes were more homogeneous. As the current increased (> 0.1 A/cm^2), more sites within the catalyst layers were utilized, resulting in a broader P2 peak that covered a wider frequency range due to the complexity of the porous anodic catalyst layer structure. Similar behavior and resistivity trends were also seen in the MEA 0.6Ir 0.1Pt in **Figure S 5** and in DRT studies in fuel cells[9,14].

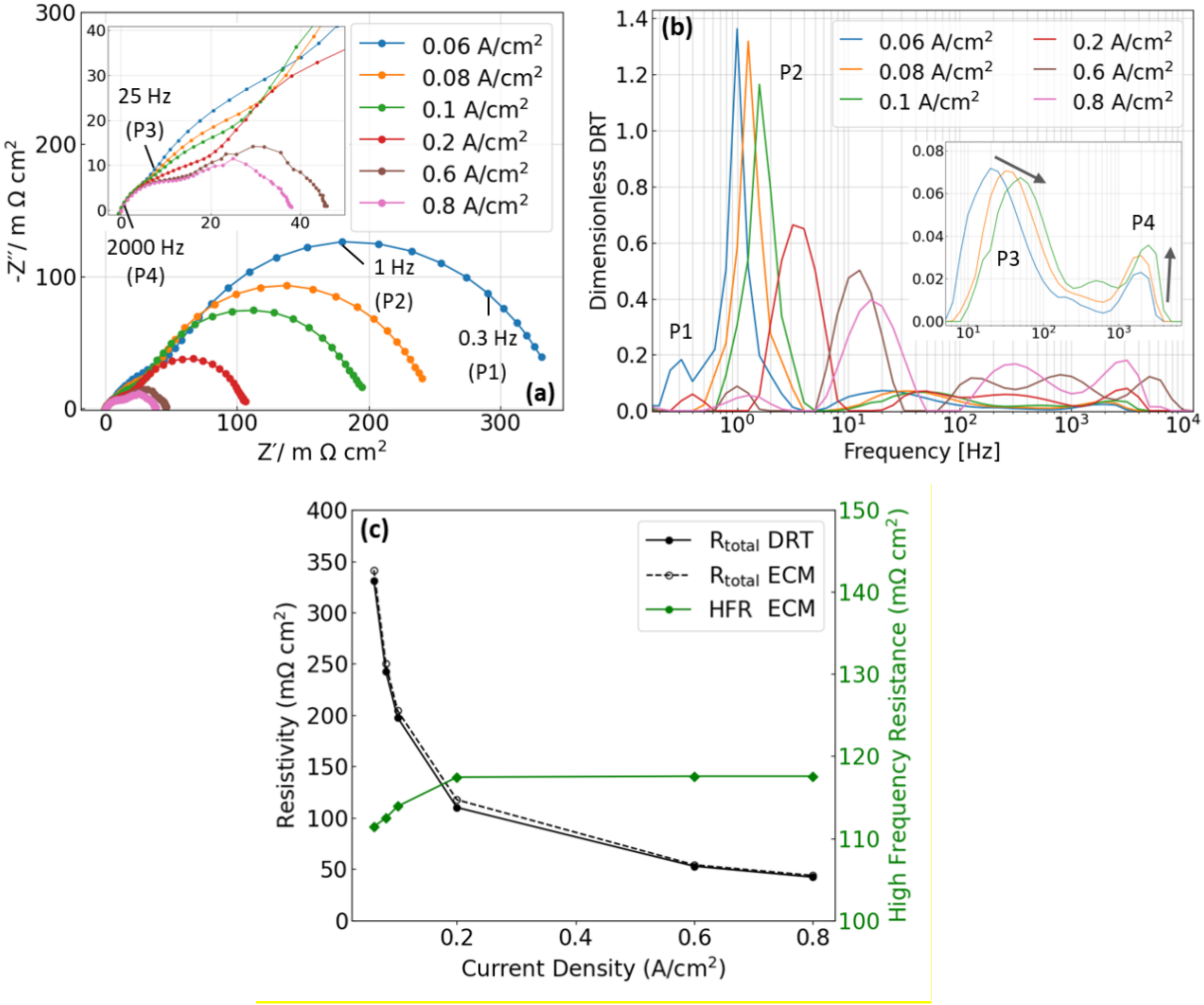
(a)
-Z″/ m Ω cm^2
Z′/ m Ω cm^2
0.06 A/cm^2
0.08 A/cm^2
0.1 A/cm^2
0.2 A/cm^2
0.6 A/cm^2
0.8 A/cm^2
25 Hz
(P3)
2000 Hz
(P4)
1 Hz
(P2)
0.3 Hz
(P1)
(b)
Dimensionless DRT
Frequency [Hz]
P1
P2
P3
P4
(c)
Resistivity (mΩ cm^2)
High Frequency Resistance (mΩ cm^2)
Current Density (A/cm^2)
R$_{total}$ DRT
R$_{total}$ ECM
HFR ECM

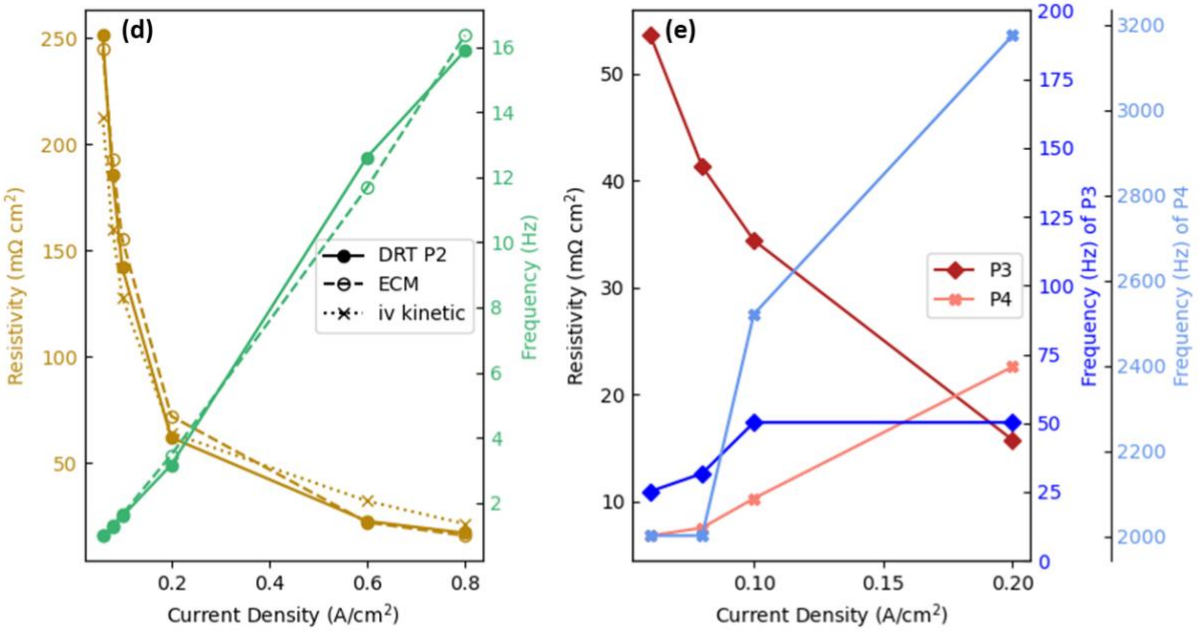

Figure 2. (a) EIS measurements from 0.06 to 0.8 A/cm^2. (b) DRT results from (a). (c) Total polarization resistance (R_{total}) obtaining from ECM or DRT. And HFR from ECM at different current densities. (d) P2 resistivity and the peak frequency from the DRT result (-●-), the resistance value from the corresponding time constant in ECM result (-o-), and the kinetic contribution from I-V curve break down analysis. (e) The resistivity and the peak frequency of P3 and P4.

DRT peaks P3 and P4 were in the range of 10 - 10^4 Hz. For current densities of 0.2 and 0.6 A/cm^2, a peak between P3 and P4 (100 and 1000 Hz) was more visible, but the processes converged into 2 peaks at 0.8 A/cm^2 in **Figure 2** (b). For this sample (MEA1.5Ir 0.1Pt), when the current density was above 0.2 A/cm^2, the peaks in the high frequency range became less isolated and more difficult to separate, which may be related to the membrane/catalyst layer hydration, causing lower site utilization that worsened proton and electron conduction[16]. Similar to the trend of P2 resistivity decreasing with increasing current density, the P3 resistivity decayed from 53.60 to 15.81 mΩcm^2 in **Figure 2(e)**, implying that P3 might be associated with other reaction steps faster than the P2 rate determining step at the anode. The corresponding results from ECM were provided in **Figure S 14 (a)**. For OER, the four reaction steps of Krasil'shchikov mechanism in an acidic environment are more broadly accepted as[31]:

(i) $S + H_2O \rightarrow S - OH + H^+ + e^-$
(ii) $S - OH \rightarrow S - O^- + H^+$
(iii) $S - O^- \rightarrow S - O + e^-$
(iv) $2S - O \rightarrow 2S + O_2$

With step (iii) as the rate determining step, the Tafel slope of the anodic reaction was approximately 47 mV/dec in previous studies [31], which was similar to those found in these MEAs (44.8 - 58.2 mV/dec). The presence of P3 in the DRT results could be due to faster OER kinetic processes, including steps (i), (ii) and (iv). While hydrogen evolution reaction (HER) kinetics may also contribute to P3, cathodic kinetics are comparatively small to PEM electrolysis overpotentials[16,21]. P3 was around 25.2 - 50.2 Hz and the resistivity decreased with increasing current density, matching the EIS trends in **Figure 2** (a) and confirming a kinetic process. While identifying P3 in DRT and separating the amounts from total impedance are beneficial to quantify this electrochemical process, this was difficult to achieve by interpreting the overlapped time constants in Nyquist plots.

P4, located at higher frequency, could be related to protonic and electronic conductivity, HER kinetics, or a combination. P4 resistivity increased with current density from 6.80 to 22.6 mΩcm^2, which can be explained by a higher number of ionic- and electronic-limited zones and thus worse catalyst utilization, mainly in the anode[16,17]. For ionic limitations specifically, increasing current shifts catalyst site utilization from the membrane interface into the catalyst layer bulk, and greater ionic resistances may occur due to the higher catalyst layer current distribution and longer ionic pathways[16]. For electronic limitations specifically, interfacial contact resistance between the PTL and catalyst layer may increase with current density, likely due to a larger area of discontinuous electric conduction of between catalyst particles and the PTL surface[21].

Throughout the current densities evaluated, P2 accounted for 71.9 - 76.5% of total resistivity at lower current density (0.06 to 0.1 A/cm^2) and 40.6 - 56.4% at higher current density (0.2 to 0.8 A/cm^2). This indicated that kinetic losses were more dominant at lower current densities and that P2 was possibly associated with the rate determining step of OER, IrO_2 hydroxide (Ir^{IV}) to IrO_2OH (Ir^{V}) [32]. P3 contributed to the total impedance with similar proportions (14.3 - 17.4%) at low current density (0.06 to 0.2 A/cm^2) and at higher currents tended to merge with other losses in the high frequency range. For EIS at 0.6 and 0.8 A/cm^2, both HFRs were around 117.6 mΩcm^2 and the difference of polarization resistance (ΔR_{total} = 10.66 mΩcm^2) was mainly due to a kinetic improvement at the higher current density (see inset plot of **Figure 2** (a)). The frequency of P2 (12.6 Hz for 0.6 A/cm^2 and 15.8 Hz for 0.8 A/cm^2) corresponded to the peak frequencies of the main polarization process in the Nyquist plot, and the resistivities at 0.6 and 0.8 A/cm^2 were 22.74 and 17.10 mΩcm^2, respectively. The peak at 317 Hz at 0.8 A/cm^2, however, also converged with the peaks related to catalyst layer protonic conductivity at a higher frequency range and were difficult to separate at this current density. Assuming that the anodic fast reactions contributed a negligible amount to the total impedance at 0.8 A/cm^2, the difference of kinetic related resistivity (ΔR_{P2} = 5.64 mΩcm^2 + ΔR_{P3} = 4.85 mΩcm^2 =10.49 mΩcm^2) was in the same range as ΔR_{total}. The sum resistivity from the peaks at 797 and 5030 Hz at 0.6 A/cm^2 was 22.94 mΩcm^2, while the sum resistivity at 0.8 A/cm^2 was slightly higher (23.23 mΩcm^2), from the peaks at 317 Hz and 3174 Hz. This phenomenon well aligned with a previous investigation, where the catalyst layer resistance increased in the low current range (< 1 A/cm^2) and reached a threshold value at higher current densities[17].

3.2.2. Effect of temperature

In this section, the effect of temperature (40, 60, and 80˚C) on the cell performance of MEA 1.5Ir 0.1Pt will be discussed. Cell efficiency increased with operating temperature due to improved kinetics (higher rate constant and lower activation energy) and lower ohmic resistance (improved proton and electron conductivity). To quantify kinetic-related processes, we focused on EIS at a low current (0.06 A/cm^2) and at three temperatures. HFRs in **Figure 3** (d) were subtracted from EIS to better illustrate differences in the Nyquist plots (**Figure 3** (b). The total polarization resistances were similar at 40 and 60˚C and increased slightly at 80˚C (24.70 and 24.71 mΩcm^2 from ECM and DRT, respectively).

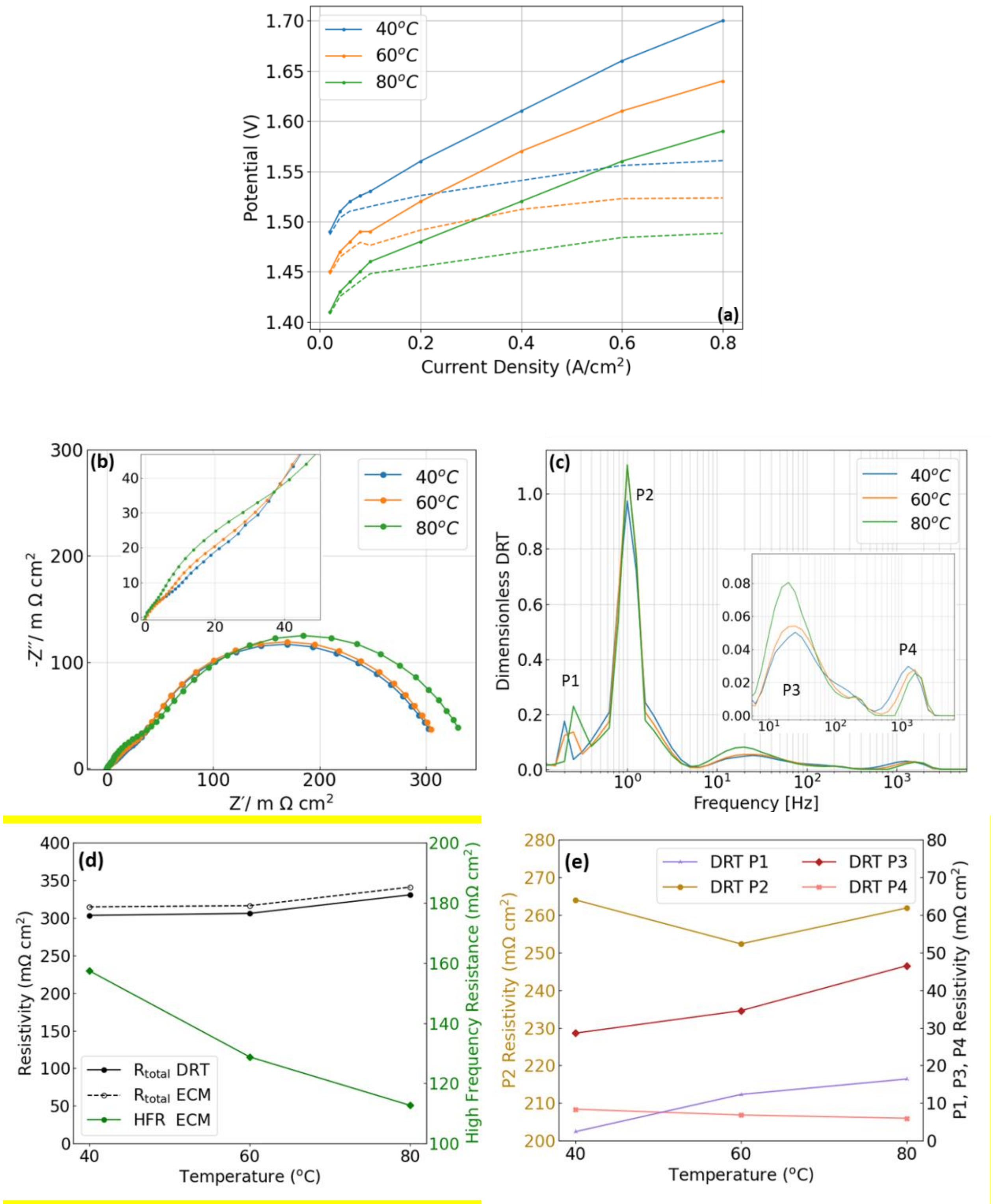

Figure 3. (a) Polarization curves at 40, 60 and 80˚C for the MEA with 1.5 mg_{Ir}/cm^2 at the anode and 0.1 mg_{Pt}/cm^2 at the cathode. Solid lines are the measured voltage. Dashed lines are HFR-free voltages. (b) Nyquist plot of EIS at 0.06 A/cm^2 at 40, 60 and 80˚C with the MEA 1.5Ir 0.1Pt. (c) DRT results of the corresponding impedance measurement. (d) Total polarization resistance from

DRT and ECM and HFR from ECM at 0.06 A/cm^2. (e) the resistivity of P1-P4 from the DRT results at 40, 60 and 80˚C.

Different mechanisms may have contributed to this trend and implementing DRT helped investigate each electrochemical process and quantify losses which dominated within different frequency ranges. In the kinetic region, the shape of P2 and P3 both slightly narrowed (lower shoulders around 1-5 Hz) with elevated temperature, possibly due to the improved reaction kinetics at higher temperature, so that primary electrochemical reactions became more dominant at specific time constants (0.06 A/cm^2 in **Figure 3** (c), 0.1 A/cm^2 in **Figure S 6.**). For the MEA with the higher anode loading (1.5 mg$_{Ir}$/cm^2), the peak frequencies were 0.25, 1.00, 25.17 and 1590 Hz for P1 - P4, respectively, and did not significantly change with temperature. The quantification of each peak was summarized in **Figure 3** (e) (ECM results in **Figure S 14 (b)**). The P2 resistivity dropped 9.15 mΩcm^2 from 40˚C to 60˚C (264.0 mΩcm^2 at 40˚C and 252.3 mΩcm^2 at 60˚C) likely because the OER kinetics improved and the charge transfer processes became more efficient. From 60˚C to 80˚C, however, greater gas production may have resulted in additional local MEA pressures, improving component/interfacial contact, or causing electrode strain which could have reduced pores and active sites in the catalyst layer and thus subtly worsened OER kinetics (261.8 mΩcm^2 at 80˚C).

The inset plot of **Figure 3** (b) showed that the impedance in the high frequency area (around 2.5 - 251 Hz) had trends of decreasing in real and imaginary parts (moves towards upper left of Nyquist plot) from 40 to 80˚C. This frequency range corresponded to P3, which had the resistivity increase with temperature (28.60, 34.56, 46.50 mΩcm^2). The corresponding time constant (R3//Q3) in ECM also showed the similar trend in **Figure S 14 (b)**. Increasing P3 resistivity could have been due to: (1) more resistance due to larger bubbles forming on the electrode surface that may have limited the amount of water in the catalyst layer at higher temperatures[15,19]; (2) faster surface oxide growth of the Ir catalyst at elevated temperature, which reduced the site reactivity[33]; and (3) changes to polymer creep modifying catalyst/ionomer interfaces, which led to decreases the electrode active area[19]. Higher ohmic resistance from the anodic catalyst layer at higher temperatures was also observed in past studies, related to a less active catalyst layer provided poor conduction for electrons and protons along the anode thickness[15,16].

From 40 to 80˚C, the resistivity of P1, related to mass transport losses, increased from 2.41 to 16.40 mΩcm^2 and the corresponding frequency slightly shifted higher due to faster transport properties at higher temperature. Past works suggested faster bubble growth rate and larger bubble size occur at higher temperature, however bubble detachment and transfer through the PTL microchannel may become more difficult on hydrophobic surfaces with higher gas generation rates[15]. Similarly, the accessibility of catalyst sites to water may be more difficult with larger bubbles or when bubbles merge on the electrode surface.

P4 contributed around 1.7 - 2.9% of total DRT resistivity and decreased from 8.39 to 5.99 mΩcm^2 with increasing temperature. This decrease may be related to the ionomer and improved proton conduction at elevated temperature, both at the catalyst layer/membrane interface and within the catalyst layers. P4 increased with current density (**Figure 2** (e)) due to the longer ion conduction pathways in the catalyst layer. The HFR further decreased with increasing temperature (**Figure 3** (d), -22.24% from 40 to 60˚C and -14.28% from 40 to 80˚C), indicating improved proton conductivity of the membrane. Moreover, the NFI measurement indicated the catalyst layer resistance decreased 18.06 % from 40 to 60˚C and 10.92 % from 60 to 80˚C (**Figure 4**), which shared a similar trend with the P4 resistivity decrease (22.25 % from 40 to 60˚C and 14.62 % from 60 to 80˚C). The methodologies of CLR approximation by linear fitting were applied from the previous work[17].

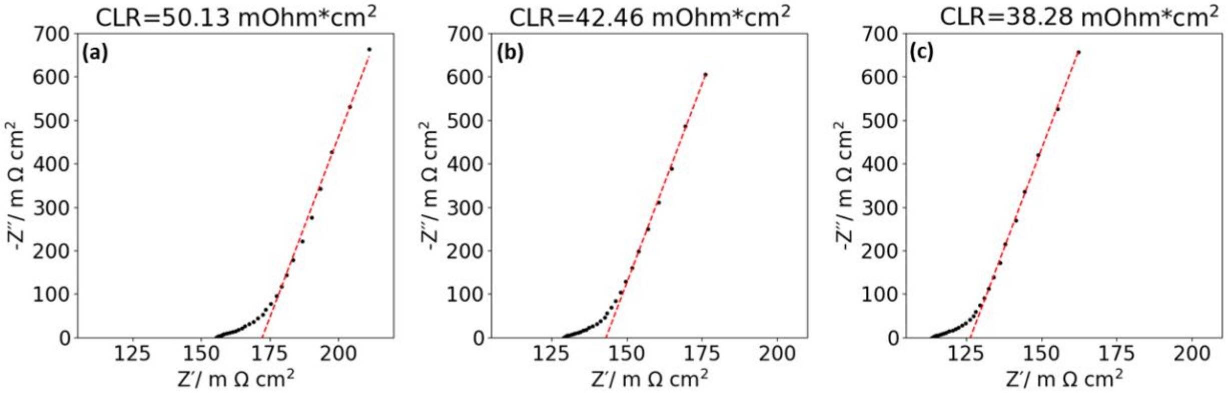

Figure 4. CLR from NFI measurement at (a) 40˚C, (b) 60˚C and (c) 80˚C.

3.2.3. Effect of loading

The performance of different catalyst loadings was investigated to better understand the 4 distinct peaks in the DRT results, and were summarized in Table 1. In **Figure 5** (a), polarization curves showed that the low cathode loading (0.035 mg_{Pt}/cm^2) had the highest overpotential in the middle and low current range, 1.65 V and 1.57 V (Hfr-free, dashed line) at 0.8 A/cm^2. Since the anode loadings of the 2 MEAs (blue and red) were both 0.2 mg_{Ir}/cm^2, the performance difference was assumed to be caused by the thin cathode of MEA 0.2Ir 0.035Pt. From the Tafel analysis, the MEA with 0.035 mg_{Pt}/cm^2 had a higher Tafel slope (58.2 mV/dec) than the MEA with 0.1 mg_{Pt}/cm^2 (49.5 mV/dec). The STEM results in **Figure 6** (a) showed the cathode with extremely low Pt loading had an uneven electrode thickness, which could result in non-uniform interfacial contact with the transport layer and suboptimal site access within the catalyst layer (compared to cathodic loading of 0.1 mg_{Pt}/cm^2 in **Figure 6** (b)). Bubbles forming in an uneven cathode may also result in mechanical stresses and local electrode deformations which may impact electrode/membrane interfaces and lessen catalyst utilization[34]. The microstructure in MEA 0.2Ir 0.035Pt cathode further showed there were more catalyst void spaces between Pt/C agglomerates which contain ionomer (from F- signal). In any case, extremely low Pt-cathode content aggravated kinetic loss, consistent with the large charge transfer resistance in EIS in **Figure 5** (c) (R_{ct} = 465.4 $m\Omega cm^2$). The ECM results of **Figure 5** (c) were summarized in **Table S 4** and **Figure S 14 (c).** In the DRT results in **Figure 5** (d), MEA 0.2Ir 0.035Pt showed that P2 and P3 overlapped and were hard to separate. This feature was also reflected in the ECM results in that the time constant of R2//Q2, R3//Q3 and R4//Q4 shared similar range of frequency (7 – 55 Hz) in **Figure S 14 (c)**. The main electrochemical process with MEA 0.2Ir 0.035Pt had slightly higher frequencies than with the standard cathode loading (MEA 0.2Ir 0.1Pt), which can be explained by the faster HER kinetics and greater HER participation in impedance that may shift kinetic-related DRT peaks to the higher frequency region. Poor kinetic performance could be related to: (1) extremely low Pt loading at the cathode slowing HER kinetics, (2) poor cathode catalyst layer uniformity indirectly impacting OER efficiency due to electron/proton movement, and (3) the nonuniform cathode resulting in poor cell compression that reduced catalyst utilization. The CV results (**Figure S 9)** showed MEA 0.2Ir 0.1Pt had a larger double layer capacitance than MEA 0.2Ir 0.035Pt, suggesting a higher degree of anode site access. For low cathode loading, DRT P2 had the highest resistivity with 445.4 $m\Omega cm^2$, shown in **Figure 5** (f), which was 117.5 $m\Omega cm^2$ higher than the MEA with 0.1 mg_{Pt}/cm^2 at the cathode. To verify the DRT results of different MEA samples, two more EIS data per sample were analyzed and the results were provided in **Figure S 13**. For MEA 0.2Ir 0.1Pt, the difference in electrode thickness, Pt particle size, catalyst/ionomer distribution and porosity were not pronounced between the pristine (**Figure S 12**) and tested samples **Figure 6** (b).

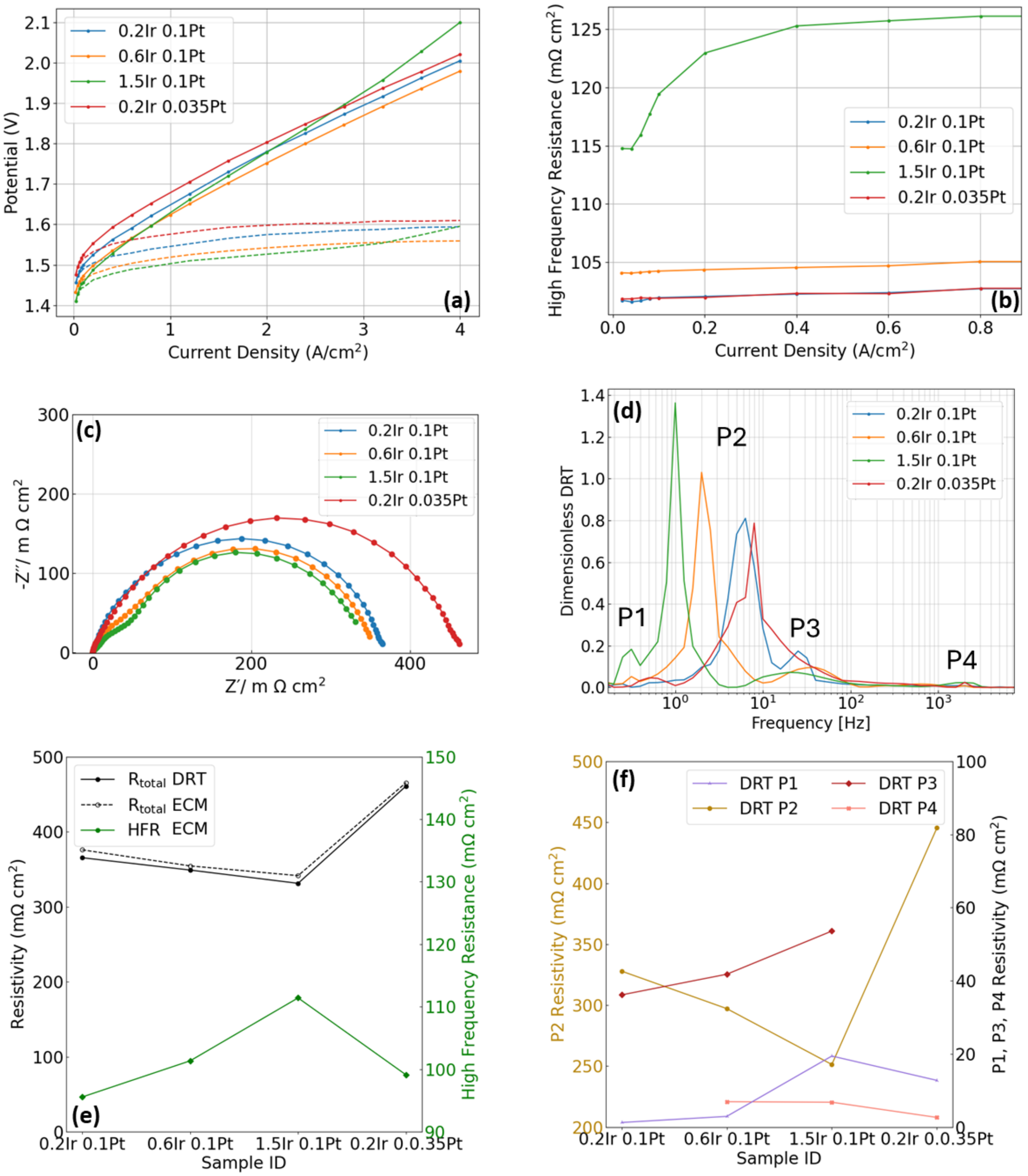

Figure 5. (a) Polarization curve of MEAs with different catalyst loadings. Solid lines are from the voltage responses at applied current densities. Dashed lines are from HFR-free voltages. (b) the relation of high frequency resistance and current densities for different MEAs. (c) EIS at 0.06 A/cm^2 with different catalyst loadings on the MEAs. (d) DRT results from EIS. (e) Polarization resistance from DRT and ECM, and HFR from ECM at 0.06 A/cm^2. (f) the resistivity of P1-P4 from the DRT results for different MEA samples.

By increasing the anode loading from 0.2 to 0.6 mg_{Ir}/cm^2, the performance improved with a lower overpotential, HFR-free voltage (**Figure 5** (a)), and Tafel slope (52.38 mV/dec in MEA 0.2Ir 0.1Pt to 44.80 mV/dec in MEA 0.6Ir 0.1Pt). The higher Ir loading likely created more active area in the catalyst layer and a more homogeneous catalyst structure, which allowed for more uniform current distribution through the catalyst layer[21]. The distance between Ir particles might be larger in MEA 0.2Ir 0,1Pt, which may have provided discontinuous electron conduction at anode/PTL interface. Through lower site access, lower Ir loading may also have accentuated catalyst migration/degradation concerns (see **Figure 7** (a)) and the isolated catalyst in the membrane negatively impacted electronic conductivity (from **Figure S 8**)[20,21]. Additionally in ECM results in **Table S 4**, the dominant time constants of higher Ir loading (0.6 mg_{Ir}/cm^2) had 3 times higher capacitance value than the low Ir loading (0.2 mg_{Ir}/cm^2). From CV measurements in **Figure S 9**, current response around 1.35 V (capacitance associated with oxide content) implied that higher Ir loading created a higher number of catalyst sites (MEA 1.5Ir 0.1Pt > MEA 0.6 Ir 0.1 Pt > MEA 0.2 Ir 0.1Pt)[18].

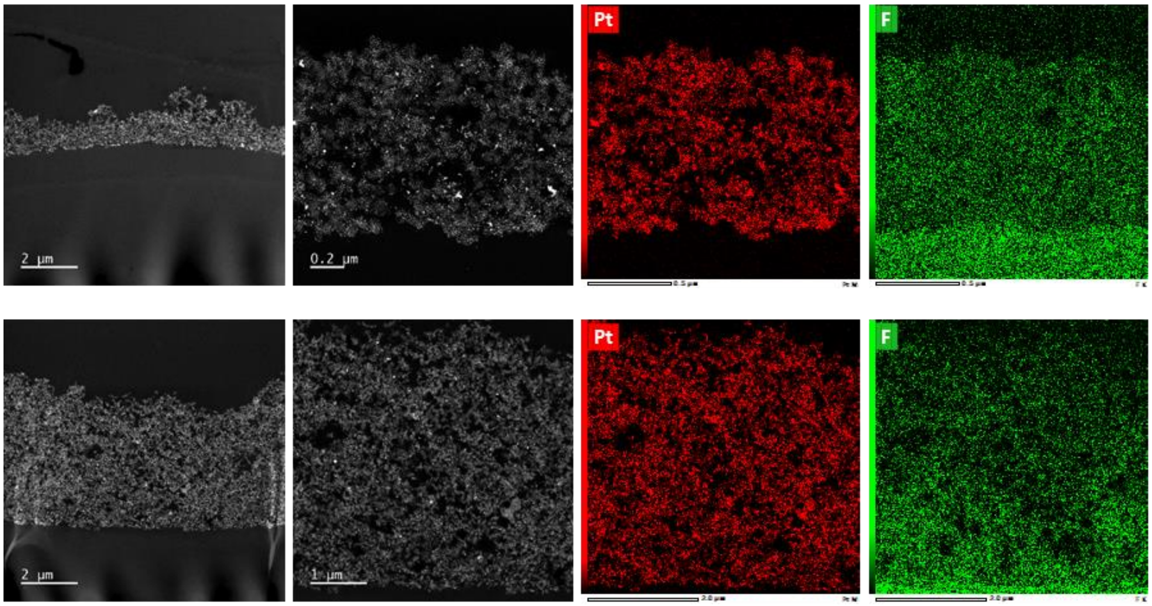

Figure 6. (a) The cathode from the tested MEA with 0.2 mg_{Ir}/cm^2 at the anode and 0.035 mg_{Pt}/cm^2 at the cathode (MEA 0.2Ir 0.035Pt). The membrane is at the bottom of the image. (b) The cathode from the tested MEA with 0.2 mg_{Ir}/cm^2 at the anode and 0.1 mg_{Pt}/cm^2 at the cathode (MEA 0.2Ir 0.1Pt).

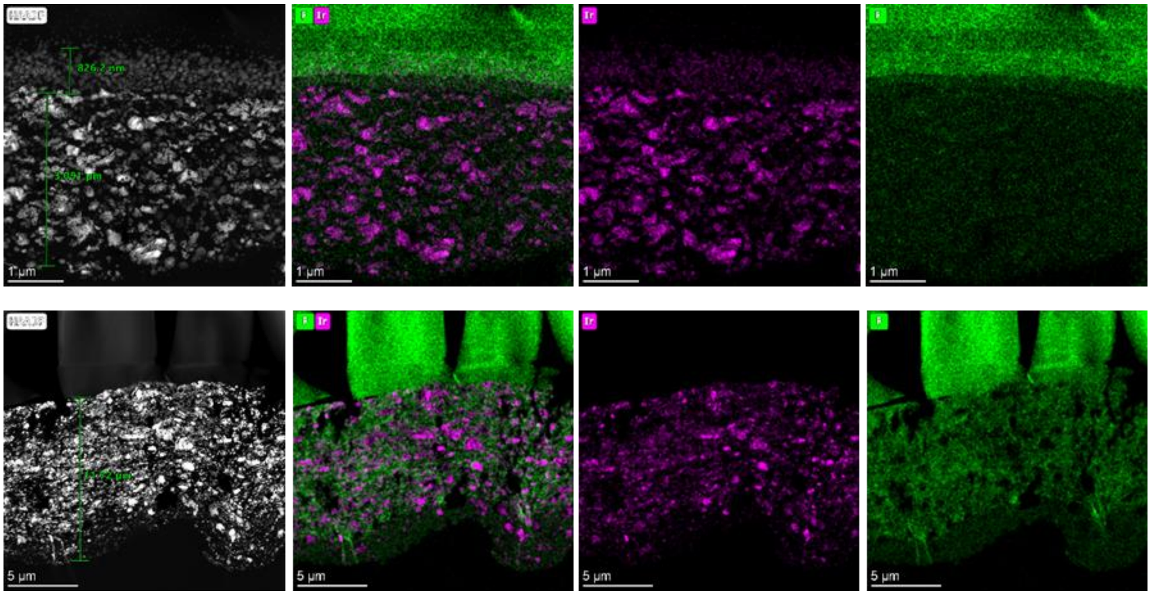

Figure 7. (a) The anode from the tested MEA with 0.2 mg_{Ir}/cm^2 at the anode and 0.1 mg_{Pt}/cm^2 at the cathode (MEA 0.2Ir 0.1Pt). The membrane is on the top of the image. (b) The anode from the tested MEA with 1.5 mg_{Ir}/cm^2 at the anode and 0.1 mg_{Pt}/cm^2 at the cathode (MEA 1.5Ir 0.1Pt). The membranes are the top of the images.

When the loading was much higher, however, the Tafel slope had a higher value (b = 58.2 mV/dec for MEA 1.5Ir 0.1Pt). A higher Tafel slope in this case likely indicated differences in electrode structure (MEA 0.2Ir 0.1Pt and MEA 1.5 Ir 0.1Pt can be seen in **Figure 7**) and not a difference in catalyst properties or intrinsic reactivity[17,20]. For low Ir loading (MEA 0.2Ir 0.1Pt), Ir mapping showed that although there were voids between Ir agglomerates, they contained ionomer (continuous fluorine signal), indicating that ionomer provided relatively homogeneous ionic conductivity within the catalyst layer. MEA 1.5Ir 0.1Pt had a more compacted structure with stronger Ir- and F- signals and less void spaces between Ir agglomerates. The inhomogeneous and discontinuous ionomer distribution was likely not ideal for proton transport and compact ionomer distribution may interfere electron conduction between Ir particles, which led to a higher CLR (38.28 $m\Omega cm^2$) in NFI measurement (see **Figure 4** (c) and **Figure S 8**).

In the DRT results, P2 resistivity decreased with higher Ir content at the anode in **Figure 5** (f), which indicated improving OER kinetics. The shifting of P2 to a lower frequency in **Figure 5** (d) may have been related to the mass transport, included in parts of P2, dragged the main process to a lower frequency range. P3, related to anodic fast reaction steps or HER (from the last sections), was more distributed and more easily separated at higher Ir loading, and its resistivity slightly increased with higher Ir contents (in a similar range 36.16 to 53.61 $m\Omega cm^2$). Similar trend from ECM results can be verified in **Figure S 14 (c)**.

P1 (mass transport) and P4 (ionic conduction) were more obvious in MEA 1.5Ir 0.1Pt. Increasing the anode loading to 1.5 mg_{Ir}/cm^2 created a thicker and less porous electrode (**Figure 7** (b)), which likely resulted in longer and more complex paths for water to supply the catalyst layer and for produced oxygen to exit to the transport layer. From EIS at 0.06 A/cm^2 (**Figure 5** (c)), the data at low frequency had a longer distance from the x axis, which implied that more transport losses occurred in the MEA with high Ir loading. In **Figure 5** (f), P1 resistivity had the highest value of 19.44 $m\Omega cm^2$. Due to the maximum current limitation of EIS instrument, EIS was taken up to 0.8 A/cm^2 (25 cm^2 cell) and future tests of cells with smaller active areas and thinner membranes could help probe mass transport effects. For P4, located in the high frequency range, the resistivity contributed to a small amount of the impedance. For MEA 1.5Ir 0.1Pt, P4 can be integrated to a resistivity of 6.96 $m\Omega cm^2$, while the MEAs with lower Ir loadings had negligible P4 resistivity. This result was in good agreement with the NFI, that MEA 1.5Ir 0.1Pt had the highest CLR (**Figure S 8**). The possible explanation are: (1) the voids in a much thicker anode were filled by O_2, which interfered with water transport and proton movement from the PTL/anode interface to anode/membrane interface[21]; and (2) the interface of Ir particles and ionomer was not ideal for proton conductivity with less water content in the thick anode[23]. Additionally in extended operation, less homogeneous proton conduction could have lessened site access in the catalyst layer and accelerated degradation on specific sections or spots in the electrode.

In **Figure 5** (c), higher HFR in MEA 1.5Ir 0.1Pt can also be attributed to worse electron conduction due to the isolation of Ir particles by compacted pore structure[23]. Moreover, for this MEA, the HFR increased with current density, while other MEAs showed that HFR was independent of current density. For anode thickness > 10 µm, similar trends of increasing HFR with current density was also found[21], and reported as due to membrane hydration at the edge of membrane/anode related to electroosmotic drag (anode to cathode)[19,21,35]. With a thicker anode, water at the surface of the electrode (PTL side) likely needed a longer path to transport to the membrane. The water content at the interface of anode and membrane was likely lower with a thick anode (high Ir loading) than with a thin anode. The increasing trend of HFR in the range of 0.2 - 0.8 A/cm^2 was less obvious because more gas production provides higher oxygen pressure at the anode, which can improve water transport and mitigate membrane hydration[21]. HFR of low Pt loading had a lower value and did not change with current density, which can be explained by lower contact resistance of a thinner MEA and the back diffusion of water from a thin cathode was easier so that the membrane was slightly more hydrated.

In **Figure 7** (a), another distinct feature was the migration of Ir, moving toward the membrane, settling at the membrane/anode interface, and forming an Ir band (around 826 nm). The pristine MEAs did not have this feature (see **Figure S 10 - S 11**). Similar anode degradation from Ir dissolution was observed in stress test of PEM electrolysis cells[34]. This could be the main reason for higher kinetic losses in MEA 0.2Ir 0.1Pt (higher values in HFR-free voltage, Tafel slope and DRT P2 resistivity), which was related to lower catalyst utilization and limited site access in the anode. For MEA 1.5Ir 0.1Pt, however, there was no Ir band or migration into the membrane, which may be due to a higher number of catalyst sites spreading operational stressors.

4. Conclusion

This study demonstrates that DRT is a promising tool in deconvoluting relaxation processes and elucidating electrolysis mechanisms for PEMECs. By preprocessing EIS data, impedance in the high frequency range can be better quantified and separated with appropriate regularization parameters in the DRT results. By varying operating current densities and temperatures, four DRT peaks were identified. P1, located at the lowest frequency range, accounts for mass transport losses. P2 and P3 are attributed to kinetic related processes and the resistivities decrease exponentially with increasing current densities. P4, associated with ionic conductivity in the high frequency region of EIS, has an increasing resistivity with higher currents and lower temperatures.

For different catalyst loadings, higher Ir loading at the anode showed more isolated polarization processes in DRT that were easier to separate from one another. The frequency of DRT peaks did not vary significantly when reducing the Pt loading from 0.1 mg_{Pt}/cm^2 to 0.035 mg_{Pt}/cm^2. High Ir loading (1.5 mg_{Ir}/cm^2) improved OER reaction kinetic due to higher number of active sites. This loading, however, also produced a compact electrode structure which resulted in poor ionic conduction of the electrode (higher catalyst layer resistance and P4 resistivity) and a less porous morphology that triggered higher mass transport losses (higher potential at 3 A/cm^2 and higher P1 resistivity). For the cathode, an extremely low Pt loading created an uneven surface which hampered charge transfer processes and reaction kinetics, possibly due to less uniform localized pressure and lower catalyst utilization in the electrode.

Applying DRT in PEMECs testing leverages advanced electrochemical diagnostic development in separating and quantifying different polarization processes. By verifying with experiment results and other modeling methods (ECM or physical models), DRT provided tremendous insights in understanding the degradation mechanisms of PEMECs during long-term operation and in developing mitigation strategies for the development of a durable, cost efficient, and high performing electrolysis system.

Acknowledgements:

This work was authored by the National Renewable Energy Laboratory, operated by Alliance for Sustainable Energy, LLC, for the U.S. Department of Energy (DOE) under Contract No. DEAC36–08GO28308. Funding provided by U.S. Department of Energy Office of Energy Efficiency and Renewable Energy, Hydrogen and Fuel Cell Technologies Office through the H2NEW Consortium. Electron microscopy research was supported by the Center for Nanophase Materials Sciences (CNMS), which is a U.S. Department of Energy, Office of Science User Facility at Oak Ridge National Laboratory.

The views expressed in the article do not necessarily represent the views of the DOE or the U.S. Government. The U.S. Government retains and the publisher, by accepting the article for publication, acknowledges that the U.S. Government retains a nonexclusive, paid-up, irrevocable, worldwide license to publish or reproduce the published form of this work, or allow others to do so, for U.S. Government purposes.

References

(1) Ayers, K.; Danilovic, N.; Ouimet, R.; Carmo, M.; Pivovar, B.; Bornstein, M. Perspectives on Low-Temperature Electrolysis and Potential for Renewable Hydrogen at Scale. *Annual Review of Chemical and Biomolecular Engineering* **2019**, *10* (Volume 10, 2019), 219–239. https://doi.org/10.1146/annurev-chembioeng-060718-030241.

(2) Carmo, M.; Fritz, D. L.; Mergel, J.; Stolten, D. A Comprehensive Review on PEM Water Electrolysis. *International Journal of Hydrogen Energy* **2013**, *38* (12), 4901–4934. https://doi.org/10.1016/j.ijhydene.2013.01.151.

(3) IRENA. Green Hydrogen Cost Reduction: Scaling up Electrolysers to Meet the 1.5C Climate Goal. *International Renewable Energy Agency, Abu Dhabi* **2020**.

(4) Buttler, A.; Spliethoff, H. Current Status of Water Electrolysis for Energy Storage, Grid Balancing and Sector Coupling via Power-to-Gas and Power-to-Liquids: A Review. *Renewable and Sustainable Energy Reviews* **2018**, *82*, 2440–2454. https://doi.org/10.1016/j.rser.2017.09.003.

(5) Dierickx, S.; Weber, A.; Ivers-Tiffée, E. How the Distribution of Relaxation Times Enhances Complex Equivalent Circuit Models for Fuel Cells. *Electrochimica Acta* **2020**, *355*, 136764. https://doi.org/10.1016/j.electacta.2020.136764.

(6) Ivers-Tiffée, E.; Weber, A. Evaluation of Electrochemical Impedance Spectra by the Distribution of Relaxation Times. *Journal of the Ceramic Society of Japan* **2017**, *125* (4), 193–201. https://doi.org/10.2109/jcersj2.16267.

(7) Kulikovsky, A. PEM Fuel Cell Distribution of Relaxation Times: A Method for the Calculation and Behavior of an Oxygen Transport Peak. *Phys. Chem. Chem. Phys.* **2020**, *22* (34), 19131–19138. https://doi.org/10.1039/D0CP02094J.

(8) Schichlein, H.; Müller, A. C.; Voigts, M.; Krügel, A.; Ivers-Tiffée, E. Deconvolution of Electrochemical Impedance Spectra for the Identification of Electrode Reaction Mechanisms in Solid Oxide Fuel Cells. *Journal of Applied Electrochemistry* **2002**, *32* (8), 875–882. https://doi.org/10.1023/A:1020599525160.

(9) Heinzmann, M.; Weber, A.; Ivers-Tiffée, E. Advanced Impedance Study of Polymer Electrolyte Membrane Single Cells by Means of Distribution of Relaxation Times. *Journal of Power Sources* **2018**, *402*, 24–33. https://doi.org/10.1016/j.jpowsour.2018.09.004.

(10) Gavrilyuk, A. L.; Osinkin, D. A.; Bronin, D. I. On a Variation of the Tikhonov Regularization Method for Calculating the Distribution Function of Relaxation Times in Impedance Spectroscopy. *Electrochimica Acta* **2020**, *354*, 136683. https://doi.org/10.1016/j.electacta.2020.136683.

(11) Gavrilyuk, A. L.; Osinkin, D. A.; Bronin, D. I. The Use of Tikhonov Regularization Method for Calculating the Distribution Function of Relaxation Times in Impedance Spectroscopy. *Russ J Electrochem* **2017**, *53* (6), 575–588. https://doi.org/10.1134/S1023193517060040.

(12) V. Schweidler, E. R. Studien Über Die Anomalien Im Verhalten Der Dielektrika. *Annalen der Physik* **1907**, *329* (14), 711–770. https://doi.org/10.1002/andp.19073291407.

(13) Fouquet, N.; Doulet, C.; Nouillant, C.; Dauphin-Tanguy, G.; Ould-Bouamama, B. Model Based PEM Fuel Cell State-of-Health Monitoring via Ac Impedance Measurements. *Journal of Power Sources* **2006**, *159* (2), 905–913. https://doi.org/10.1016/j.jpowsour.2005.11.035.

(14) Kulikovsky, A. A Kernel for Calculating PEM Fuel Cell Distribution of Relaxation Times. *Front. Energy Res.* **2021**, *9*. https://doi.org/10.3389/fenrg.2021.780473.

(15) Li, Y.; Kang, Z.; Mo, J.; Yang, G.; Yu, S.; Talley, D. A.; Han, B.; Zhang, F.-Y. *In-Situ* Investigation of Bubble Dynamics and Two-Phase Flow in Proton Exchange Membrane Electrolyzer Cells. *International Journal of Hydrogen Energy* **2018**, *43* (24), 11223–11233. https://doi.org/10.1016/j.ijhydene.2018.05.006.

(16) Kang, Z.; Wang, H.; Liu, Y.; Mo, J.; Wang, M.; Li, J.; Tian, X. Exploring and Understanding the Internal Voltage Losses through Catalyst Layers in Proton Exchange Membrane Water Electrolysis Devices. *Applied Energy* **2022**, *317*, 119213. https://doi.org/10.1016/j.apenergy.2022.119213.

(17) Padgett, E.; Bender, G.; Haug, A.; Lewinski, K.; Sun, F.; Yu, H.; Cullen, D. A.; Steinbach, A. J.; Alia, S. M. Catalyst Layer Resistance and Utilization in PEM Electrolysis. *J. Electrochem. Soc.* **2023**, *170* (8), 084512. https://doi.org/10.1149/1945-7111/acee25.

(18) Pfeifer, V.; Jones, T. E.; Vélez, J. J. V.; Arrigo, R.; Piccinin, S.; Hävecker, M.; Knop-Gericke, A.; Schlögl, R. In Situ Observation of Reactive Oxygen Species Forming on Oxygen-Evolving Iridium Surfaces. *Chem. Sci.* **2017**, *8* (3), 2143–2149. https://doi.org/10.1039/C6SC04622C.

(19) Kai, J.; Saito, R.; Terabaru, K.; Li, H.; Nakajima, H.; Ito, K. Effect of Temperature on the Performance of Polymer Electrolyte Membrane Water Electrolysis: Numerical Analysis of Electrolysis Voltage Considering Gas/Liquid Two-Phase Flow. *J. Electrochem. Soc.* **2019**, *166* (4), F246. https://doi.org/10.1149/2.0521904jes.

(20) Hegge, F.; Lombeck, F.; Cruz Ortiz, E.; Bohn, L.; von Holst, M.; Kroschel, M.; Hübner, J.; Breitwieser, M.; Strasser, P.; Vierrath, S. Efficient and Stable Low Iridium Loaded Anodes for PEM Water Electrolysis Made Possible by Nanofiber Interlayers. *ACS Appl. Energy Mater.* **2020**, *3* (9), 8276–8284. https://doi.org/10.1021/acsaem.0c00735.

(21) Bernt, M.; Siebel, A.; Gasteiger, H. A. Analysis of Voltage Losses in PEM Water Electrolyzers with Low Platinum Group Metal Loadings. *J. Electrochem. Soc.* **2018**, *165* (5), F305. https://doi.org/10.1149/2.0641805jes.

(22) Li, Y.; Jiang, Y.; Dang, J.; Deng, X.; Liu, B.; Ma, J.; Yang, F.; Ouyang, M.; Shen, X. Application of Distribution of Relaxation Times Method in Polymer Electrolyte Membrane Water Electrolyzer. *Chemical Engineering Journal* **2023**, *451*, 138327. https://doi.org/10.1016/j.cej.2022.138327.

(23) Bernt, M.; Gasteiger, H. A. Influence of Ionomer Content in IrO $_2$ /TiO $_2$ Electrodes on PEM Water Electrolyzer Performance. *J. Electrochem. Soc.* **2016**, *163* (11), F3179–F3189. https://doi.org/10.1149/2.0231611jes.

(24) Bender, G.; Carmo, M.; Smolinka, T.; Gago, A.; Danilovic, N.; Mueller, M.; Ganci, F.; Fallisch, A.; Lettenmeier, P.; Friedrich, K. A.; Ayers, K.; Pivovar, B.; Mergel, J.; Stolten, D. Initial Approaches in Benchmarking and Round Robin Testing for Proton Exchange Membrane Water Electrolyzers. *International Journal of Hydrogen Energy* **2019**, *44* (18), 9174–9187. https://doi.org/10.1016/j.ijhydene.2019.02.074.

(25) Murbach, M. D.; Gerwe, B.; Dawson-Elli, N.; Tsui, L. Impedance.Py: A Python Package for Electrochemical Impedance Analysis. *Journal of Open Source Software* **2020**, *5* (52), 2349. https://doi.org/10.21105/joss.02349.

(26) Hahn, M.; Schindler, S.; Triebs, L.-C.; Danzer, M. A. Optimized Process Parameters for a Reproducible Distribution of Relaxation Times Analysis of Electrochemical Systems. *Batteries* **2019**, *5* (2), 43. https://doi.org/10.3390/batteries5020043.

(27) Shin, E.-C.; Ahn, P.-A.; Seo, H.-H.; Jo, J.-M.; Kim, S.-D.; Woo, S.-K.; Yu, J. H.; Mizusaki, J.; Lee, J.-S. Polarization Mechanism of High Temperature Electrolysis in a Ni–YSZ/YSZ/LSM Solid Oxide Cell by Parametric Impedance Analysis. *Solid State Ionics* **2013**, *232*, 80–96. https://doi.org/10.1016/j.ssi.2012.10.028.

(28) Franzetti, I.; Pushkarev, A.; Chan, A.-L.; Smolinka, T. Parasitic Effects in Impedance Spectrum of PEM Water Electrolysis Cells: Case Study of High-Frequency Inductive Effects. *Energy Technology* **2023**, *11* (12), 2300375. https://doi.org/10.1002/ente.202300375.

(29) Hsu, C. H.; Mansfeld, F. ***Technical Note:*** Concerning the Conversion of the Constant Phase Element Parameter Y $_0$ into a Capacitance. *CORROSION* **2001**, *57* (9), 747–748. https://doi.org/10.5006/1.3280607.

(30) Erinmwingbovo, C.; La Mantia, F. Estimation and Correction of Instrument Artefacts in Dynamic Impedance Spectra. *Sci Rep* **2021**, *11* (1), 1362. https://doi.org/10.1038/s41598-020-80468-x.

(31) Damjanovic, A.; Dey, A.; Bockris, J. O. Kinetics of Oxygen Evolution and Dissolution on Platinum Electrodes. *Electrochimica Acta* **1966**, *11* (7), 791–814. https://doi.org/10.1016/0013-4686(66)87056-1.

(32) Cherevko, S.; Geiger, S.; Kasian, O.; Mingers, A.; Mayrhofer, K. J. J. Oxygen Evolution Activity and Stability of Iridium in Acidic Media. Part 2. – Electrochemically Grown Hydrous Iridium Oxide. *Journal of Electroanalytical Chemistry* **2016**, *774*, 102–110. https://doi.org/10.1016/j.jelechem.2016.05.015.

(33) Alia, S. M.; Ha, M.-A.; Anderson, G. C.; Ngo, C.; Pylypenko, S.; Larsen, R. E. The Roles of Oxide Growth and Sub-Surface Facets in Oxygen Evolution Activity of Iridium and Its Impact on Electrolysis. *J. Electrochem. Soc.* **2019**, *166* (15), F1243. https://doi.org/10.1149/2.0771915jes.

(34) Alia, S. M.; Reeves, K. S.; Cullen, D. A.; Yu, H.; Kropf, A. J.; Kariuki, N.; Park, J. H.; Myers, D. J. Simulated Start-Stop and the Impact of Catalyst Layer Redox on Degradation

and Performance Loss in Low-Temperature Electrolysis. *J. Electrochem. Soc.* **2024**, *171* (4), 044503. https://doi.org/10.1149/1945-7111/ad2bea.

(35) Springer, T. E.; Zawodzinski, T. A.; Gottesfeld, S. Polymer Electrolyte Fuel Cell Model. *J. Electrochem. Soc.* **1991**, *138* (8), 2334–2342. https://doi.org/10.1149/1.2085971.

Supplement

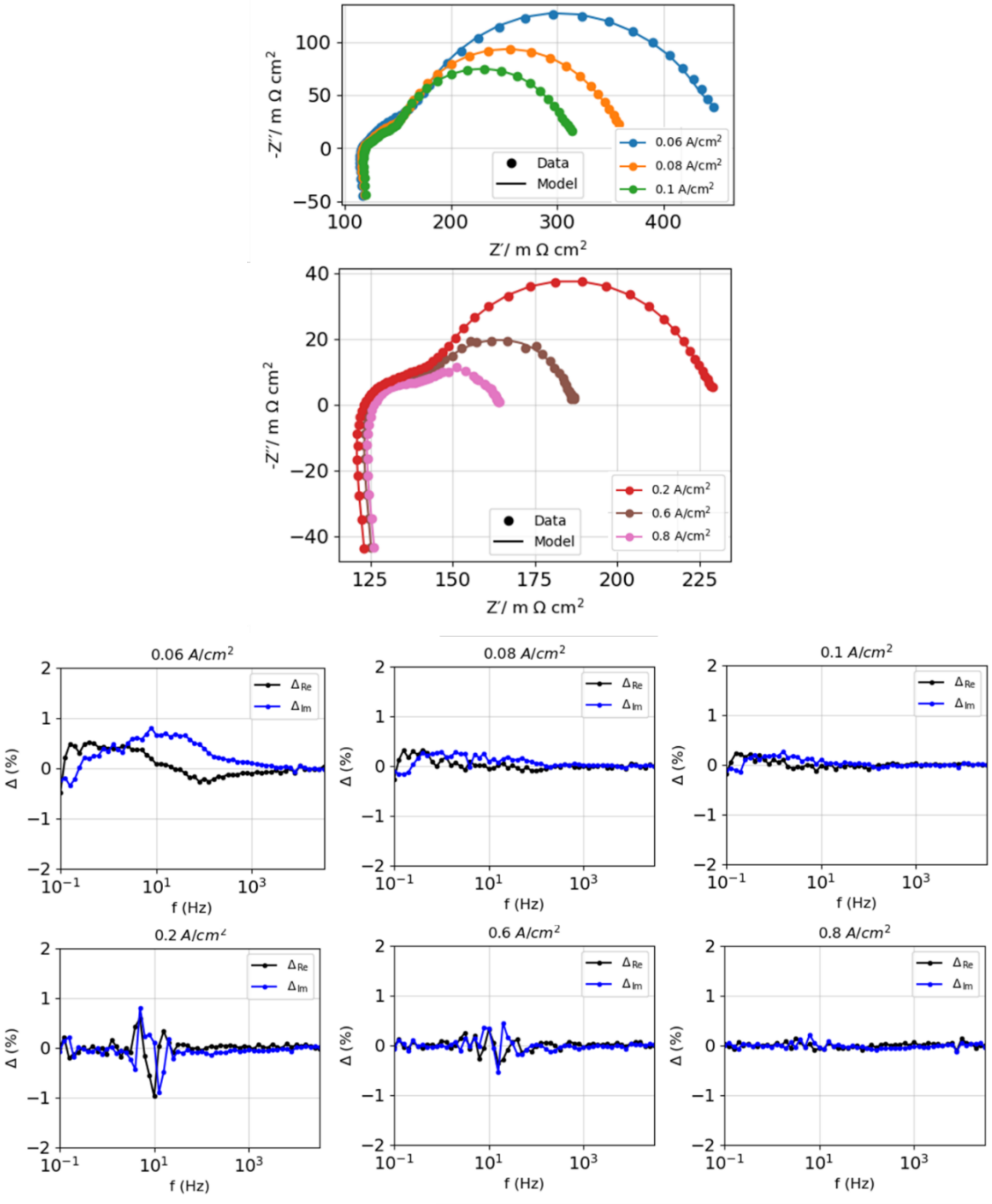

Figure S 1. KK test results from EIS at 0.06 to 0.8 A/cm^2 at 80 °C with the MEA 1.5 Ir 0.1Pt (1.5 mg$_{Ir}$/cm^2 at the anode and 0.1 mg$_{Pt}$/cm^2 at the cathode).

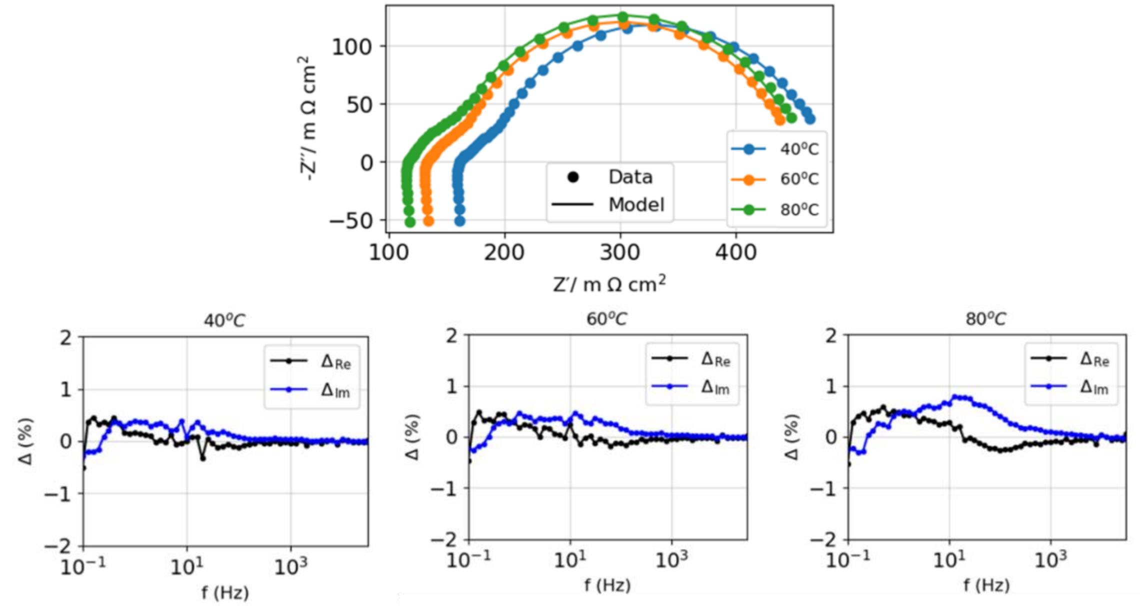

Figure S 2. KK test results from EIS at 0.06 A/cm^2 at 40 to 80 ^{o}C with the MEA 1.5 Ir 0.1Pt (1.5 mg$_{Ir}$/cm^2 at the anode and 0.1 mg$_{Pt}$/cm^2 at the cathode).

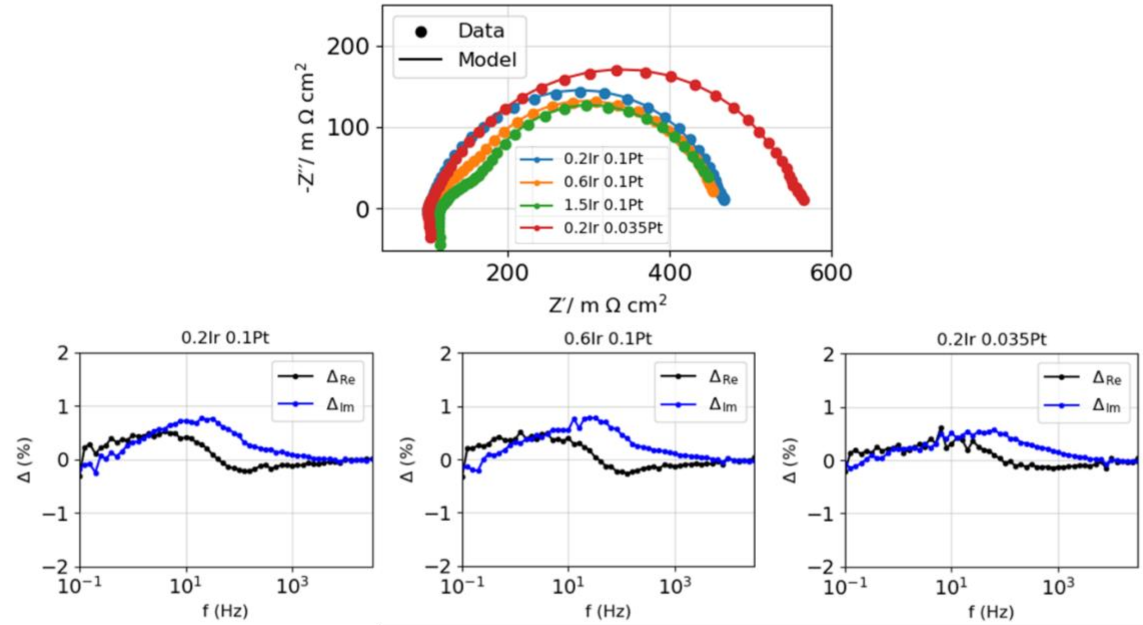

Figure S 3. KK test results from EIS at 0.06 A/cm^2, 80 ^{o}C with the MEA 0.2Ir 0.1Pt, MEA 0.6 Ir 0.1Pt and MEA 0.2 Ir 0.035Pt. KK test result of MEA 1.5Ir 0.1Pt was presented in Fig S1.

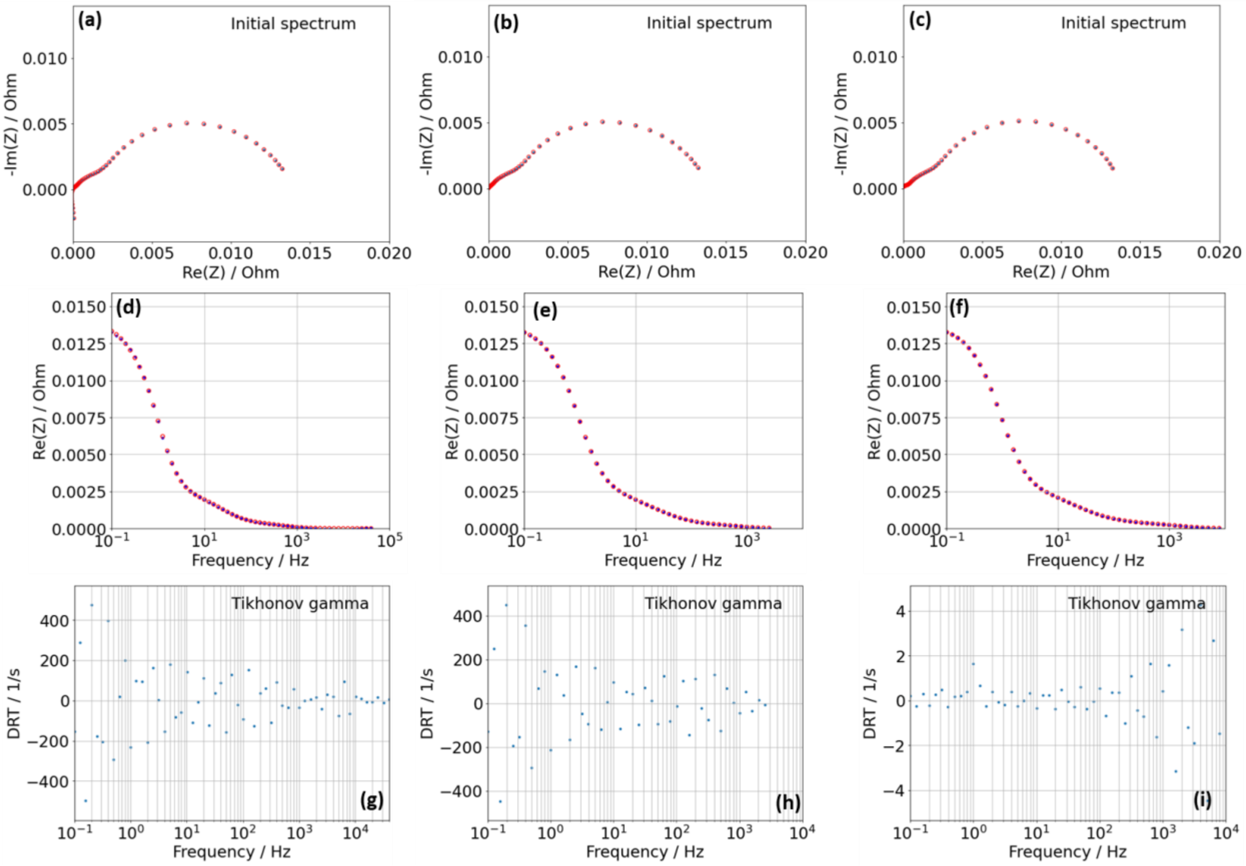

Figure S 4. DRT results by using raw data ((a), (d) and (g)), cut-off approach (b), (e) and (h) and model-and -remove approach (c), (f) and (i). Experiment data is in blue points and modeled impedance is in red circle for (a)-(f). The initial gamma function $\gamma(f)$ from the DRT algorithms, (g)-(i).

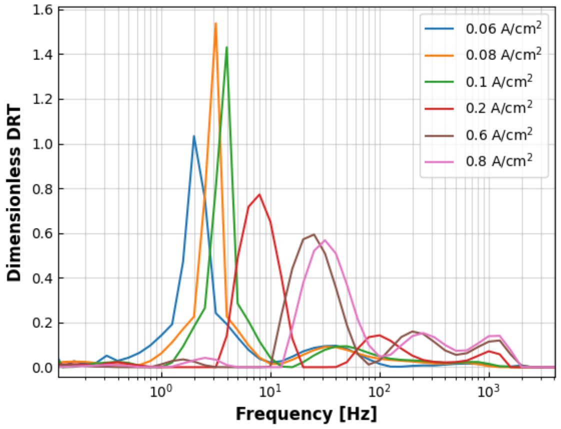

Figure S 5. DRT results of MEA with 0.6 mg$_{Ir}$/cm^2 at the anode and 0.1 mg$_{Pt}$/cm^2 at the cathode) from EIS at 0.06 A/cm^2 to 0.8 A/cm^2

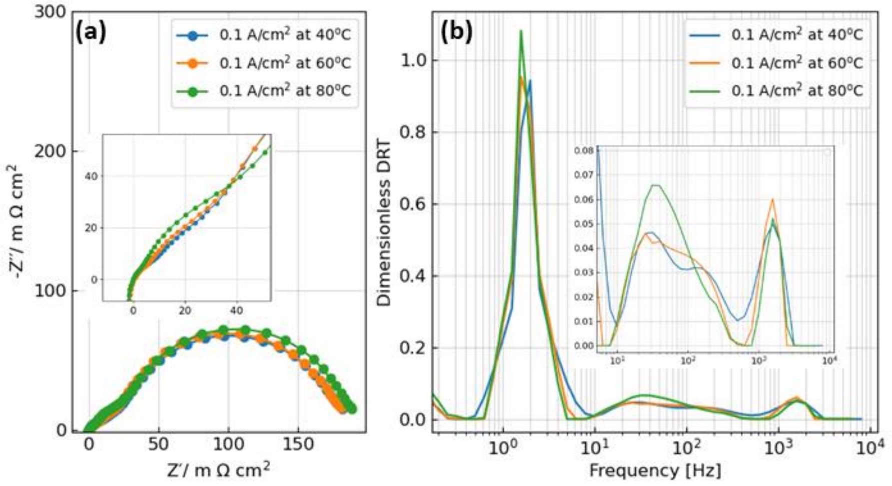

Figure S 6. (a) Nyquist plot of EIS at 0.1 A/cm^2 at 40˚C, 60˚C and 80˚C with the MEA 1.5Ir 0.1Pt. (b) DRT results of the corresponding impedance measurement.

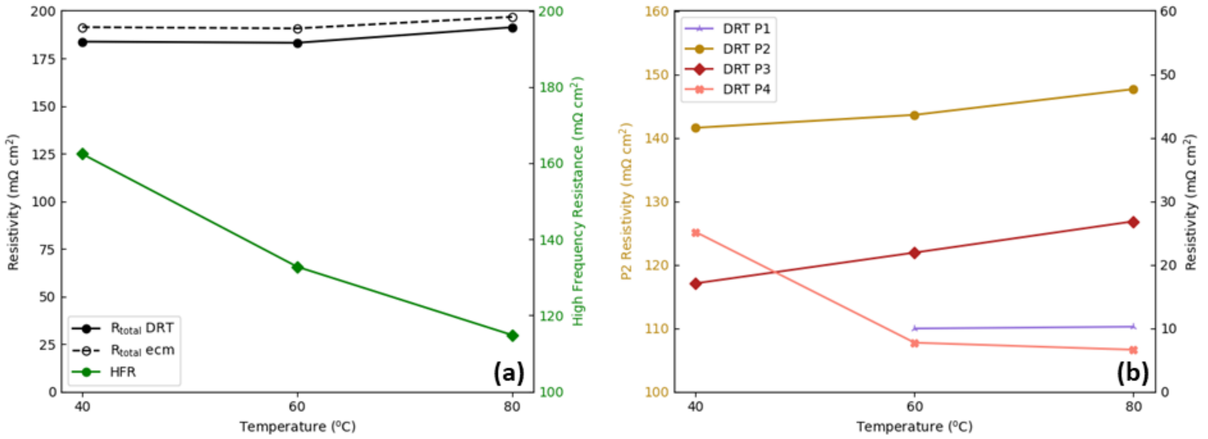

Figure S 7. (a) Total polarization resistance and high frequency resistance from EIS at 0.1 A/cm^2 with the MEA 1.5Ir 0.1Pt. (b) the resistivity of P1-P4 from the DRT results at 40˚C, 60˚C and 80˚C.

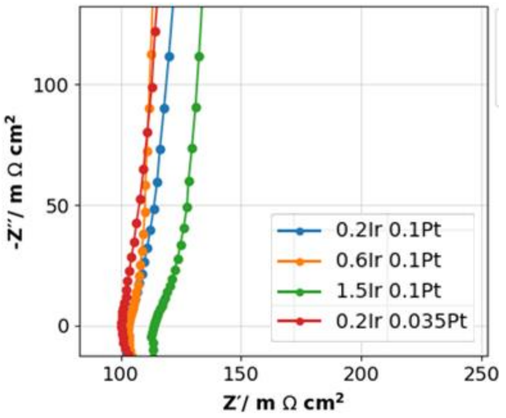

Figure S 8. Non-faradaic impedance (NFI) of different MEA loadings.

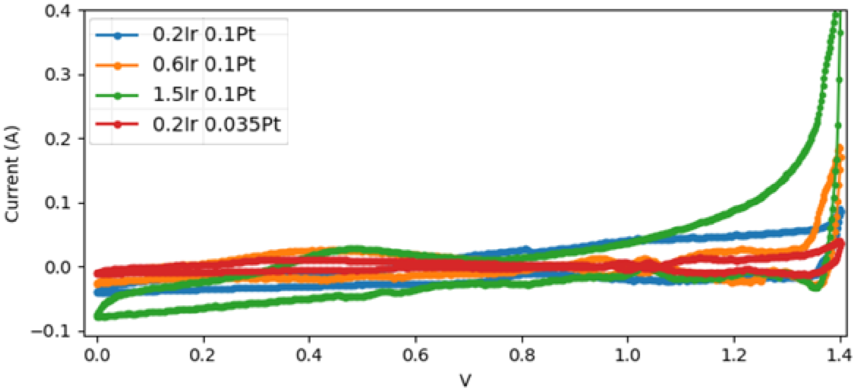

Figure S 9. Cyclic voltammetry of different MEA samples.

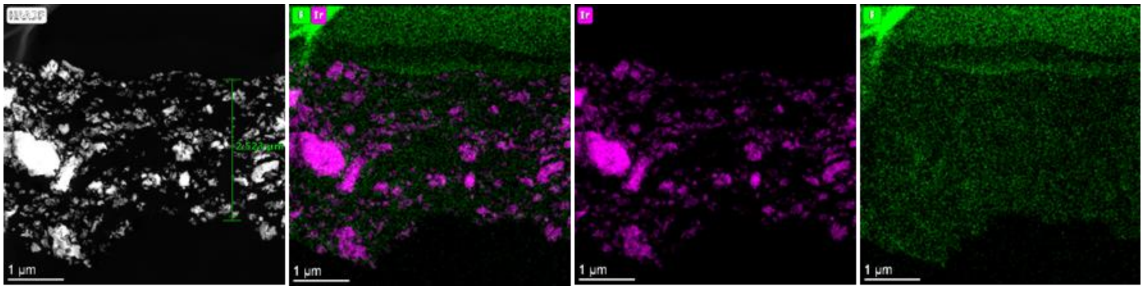

Figure S 10. The anode from the pristine sample of MEA with 0.2 mg$_{Ir}$/cm^2 and 0.1 mg$_{Pt}$/cm^2 at the anode and the cathode (MEA 0.2Ir 0.1Pt). The membrane is on the top of the image.

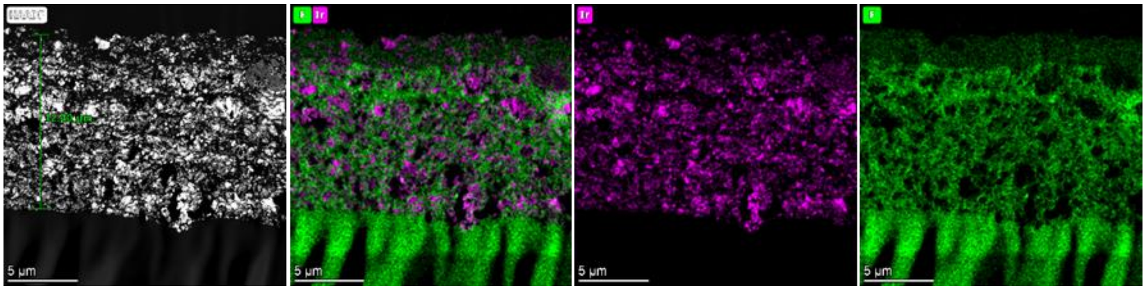

Figure S 11. The anode from the pristine sample of MEA with 1.5mg$_{Ir}$/cm^2 and 0.1 mg$_{Pt}$/cm^2 at the anode and the cathode (MEA 1.5Ir 0.1Pt). The membrane is at the bottom of the image.

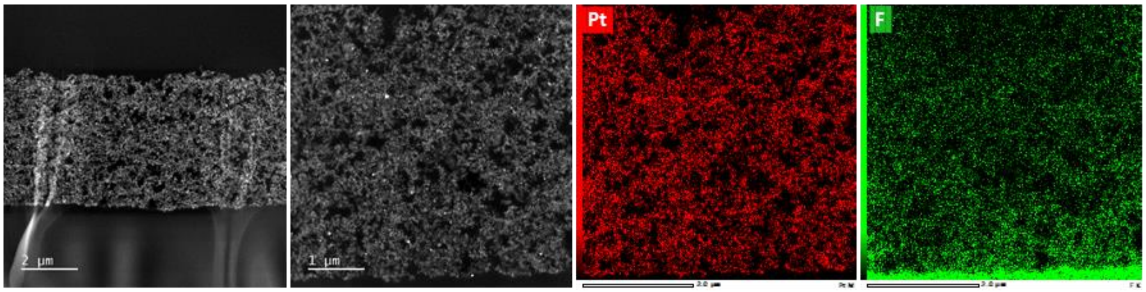

Figure S 12. The cathode from the pristine sample of MEA with $0.2 mg_{Ir}/cm^2$ and 0.1 mg_{Pt}/cm^2 at the anode and the cathode (MEA 0.2Ir 0.1Pt). The membrane is at the bottom of the image.

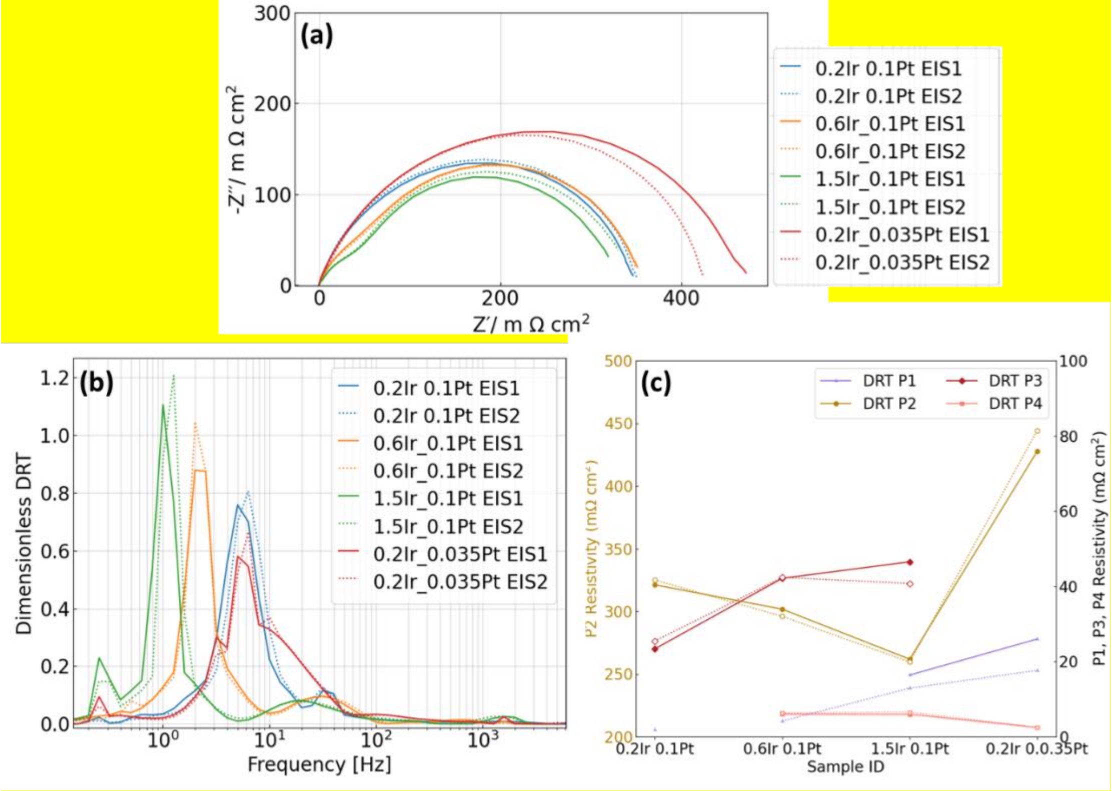

Figure S 13. (a) Nyquist plot of EIS at $0.06 A/cm^2$ for different MEA samples. (b) DRT results of the corresponding impedance measurement. (c) the resistivity of P1-P4 from the DRT results in (b). The solid lines are EIS1 and the dotted lines are EIS2.

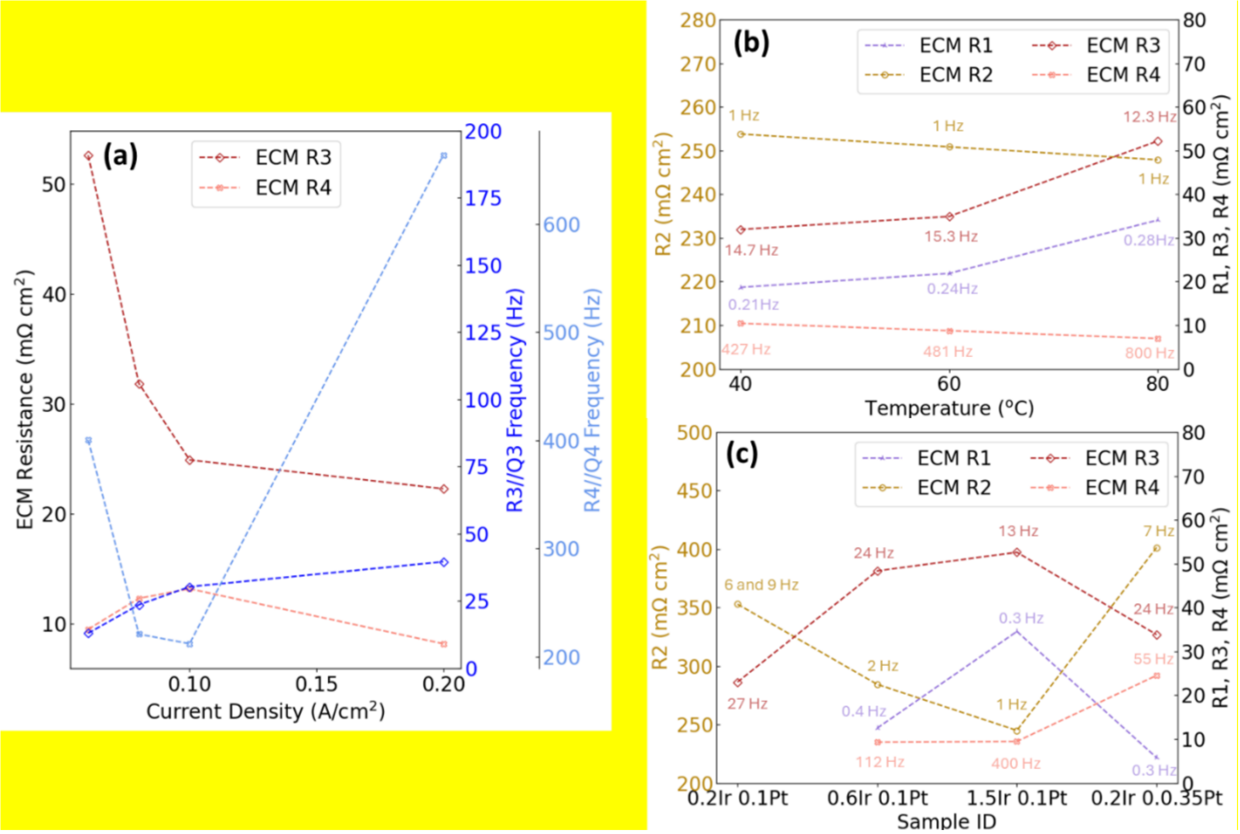

Figure S 14. The ECM results correspond to (a) different current density in **Figure 2 (e).** (b) different temperatures in **Figure 3 (e)**. (c) effect of catalyst loadings in **Figure 5 (f)**

Table S 1. Parameters obtained during DRT algorithms by using different data preprocessing methods.

DRT results from different methods	Raw data	Cut-Off	Model-and-remove
R_{pol}(mΩcm^2)	329	331	331
λ_T	1.98e-14	5.48e-13	2.97e-13
λ_{PG}	7.12e-03	1.98e-02	2.00e-02
Initial Tikhonov residual	1.77e-10	7.73e-11	9.32e-13
Final Tikhonov residual	4.80e-02	2.23e-04	1.25e-04
P1 frequency (Hz)	0.20	0.20	0.32
P1 resistivity (mΩcm2)	40.37	30.09	20.06
P2 frequency (Hz)	1.00	1.00	1.00
P2 resistivity (mΩcm2)	231	245	250

P3 frequency (Hz)	25.17	25.17	19.99
P3 resistivity (mΩcm2)	48.77	49.30	53.73
P4 frequency (Hz)	797	797	2002
P4 resistivity (mΩcm2)	9.38	6.38	6.87

Table S 2. The ECM results of EIS at 0.06 – 0.8 A/cm^2 at 80 ^{o}C for MEA1.5Ir0.1Pt.

Circuit element	0.06 A/cm^2	0.08 A/cm^2	0.1 A/cm^2	0.2 A/cm^2	0.6 A/cm^2	0.8 A/cm^2
L_α	9.59e-06	9.60e-06	9.57e-06	9.47e-06	9.42e-06	9.37E-06
α	0.93	0.93	0.93	0.93	0.93	0.93
R_{ohm}	4.46	4.50	4.56	4.70	4.78	4.83
R_1	0.38	0.49	0.52	0.33	0.087	0.12
Q_1	1.50e-03	2.54e-03	2.70e-03	1.32e-03	5.29e-04	3.33e-4
n_1	0.80	0.73	0.72	0.80	1.00	0.999
R_2	2.10	1.27	0.99	0.89	0.97	0.78
Q_2	8.47e-03	7.35e-03	7.62e-03	1.16e-2	7.93e-03	4.86e-3
n_2	0.79	0.84	0.84	0.68	0.62	0.70
R_3	9.80	7.73	6.22	2.88	0.91	0.63
Q_3	1.76e-02	1.73e-02	1.71e-02	1.76e-02	1.49e-2	1.54e-2
n_3	0.96	0.96	0.96	0.96	1.00	1.00
R_4	1.38	0.52	0.43	0.60	0.11	0.21
Q_4	0.42	1.65	2.55	1.36	1.22	0.59
n_4	1.00	1.00	1.00	0.47	0.96	0.68
X^2	1.85e-3	3.09e-4	1.79e-4	7.14e-5	3.11e-4	2.48e-4

$$X^2 = \sum_{n=0}^{N} \frac{1}{|Z|}\left[Z'_{data}(\omega_n) - Z'_{model}(\omega_n)\right]^2 + \left[Z''_{data}(\omega_n) - Z''_{model}(\omega_n)\right]^2$$

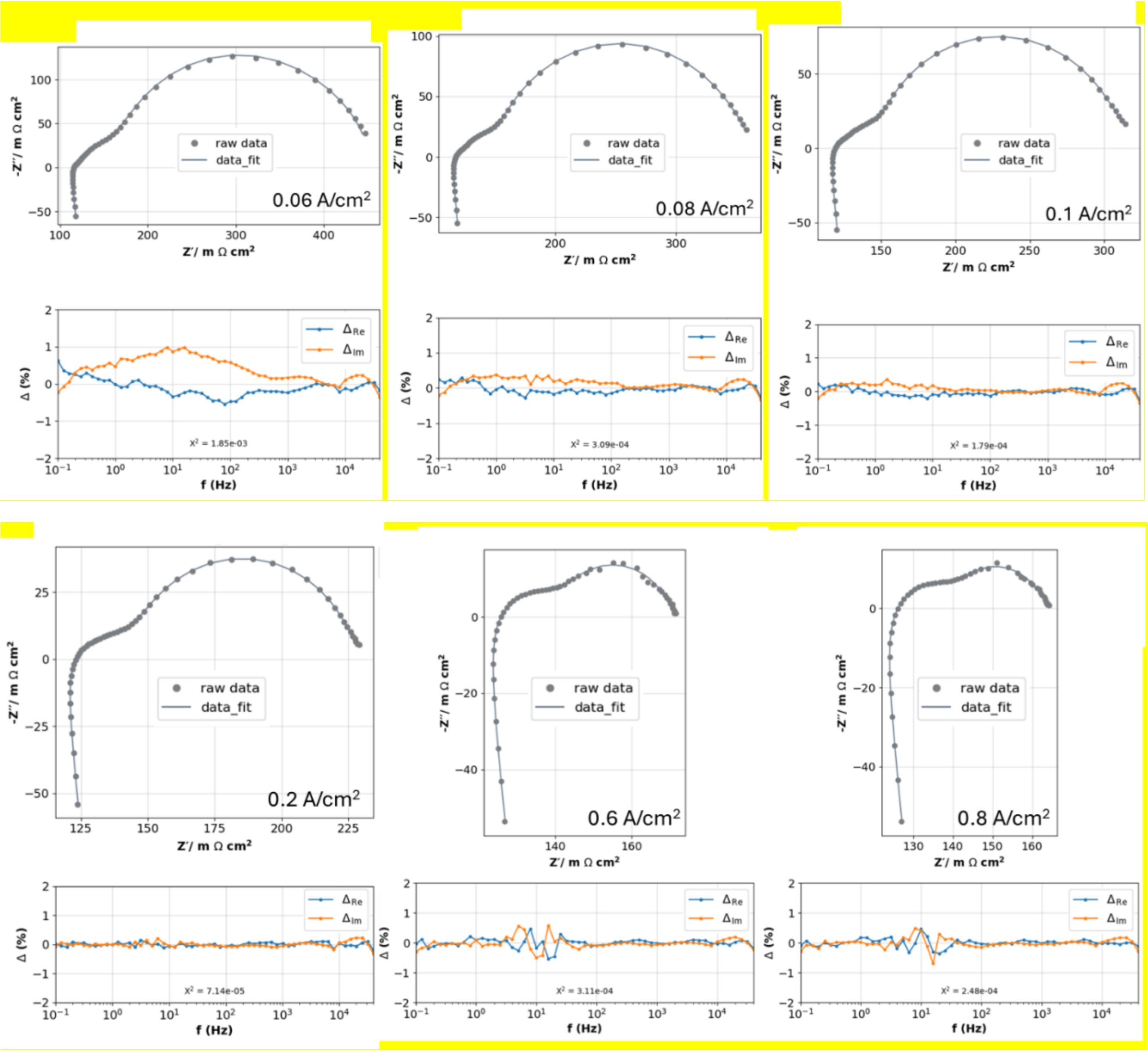

Table S 3. The ECM results of EIS at 40 – 80 °C at 0.06 A/cm^2 for MEA1.5Ir0.1Pt.

Circuit element	40 °C	60 °C	80 °C
L_α	1.06e-05	1.07e-05	1.10e-05
α	0.96	0.94	0.94
R_{ohm}	6.30	5.15	4.15
R_1	0.42	0.35	0.28
Q_1	1.19e-03	1.27e-03	8.99e-04

n_1	0.84	0.84	0.88
R_2	1.28	1.40	2.09
Q_2	1.27e-02	1.06e-02	8.83e-03
n_2	0.78	0.81	0.81
R_3	10.15	10.03	9.92
Q_3	1.73e-02	1.70e-02	1.69e-02
n_3	0.92	0.94	0.95
R_4	0.75	0.87	1.36
Q_4	1.02	0.76	0.42
n_4	1.00	1.00	1.00
X^2	6.57e-4	8.69e-4	2.01e-3

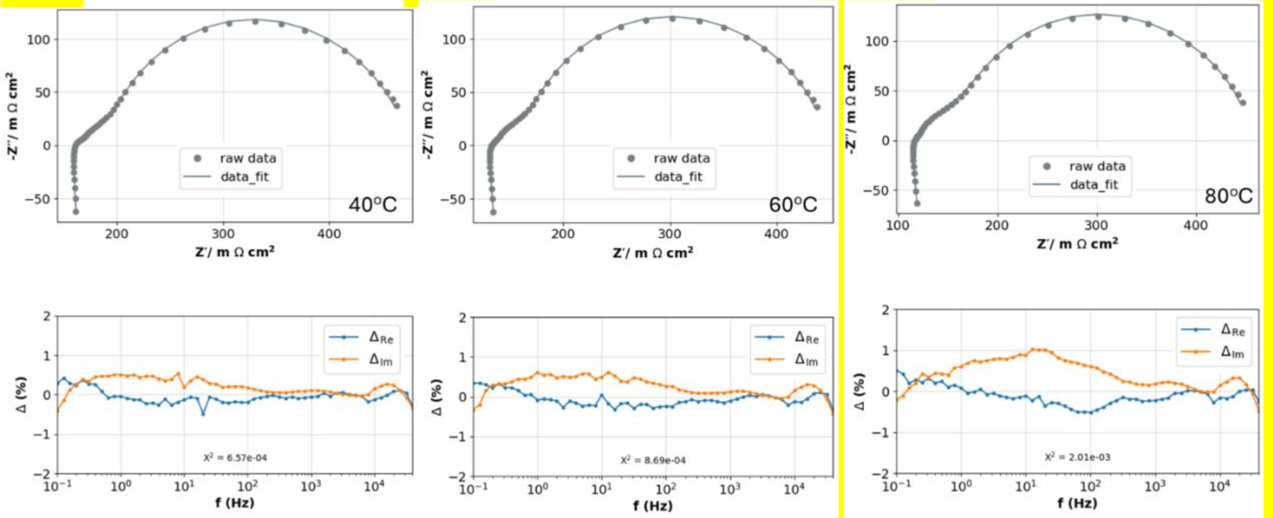

Table S 4. The ECM results of EIS at 0.06 A/cm^2, 80 °C for different catalyst loadings.

Circuit element	MEA0.2Ir 0.1Pt	MEA0.6Ir 0.1Pt	MEA1.5Ir 0.1Pt	MEA0.2Ir 0.035Pt
L_α	5.18e-06	7.04e-06	9.59e-06	7.68e-06
α	0.82	0.91	0.93	0.91
R_{ohm}	3.82	4.05	4.46	3.96
R_1	0.92	0.37	0.38	0.98
Q_1	6.38e-03	8.23e-03	1.50e-03	1.10e-03
n_1	1.00	0.69	0.80	0.66
R_2	1.37	1.93	2.10	1.35
Q_2	1.55e-01	4.61e-03	8.47e-03	6.66e-03
n_2	0.32	0.88	0.79	0.92
R_3	12.74	11.37	9.80	16.05
Q_3	2.99e-03	7.96e-03	1.76e-02	2.43e-03

n_3	0.90	0.92	0.96	0.86
R_4	-	0.87	1.38	1.38
Q_4	-	0.76	0.42	0.42
n_4	-	1.00	1.00	1.00
X^2	2.02e-3	1.68e-3	1.85e-3	1.36e-3

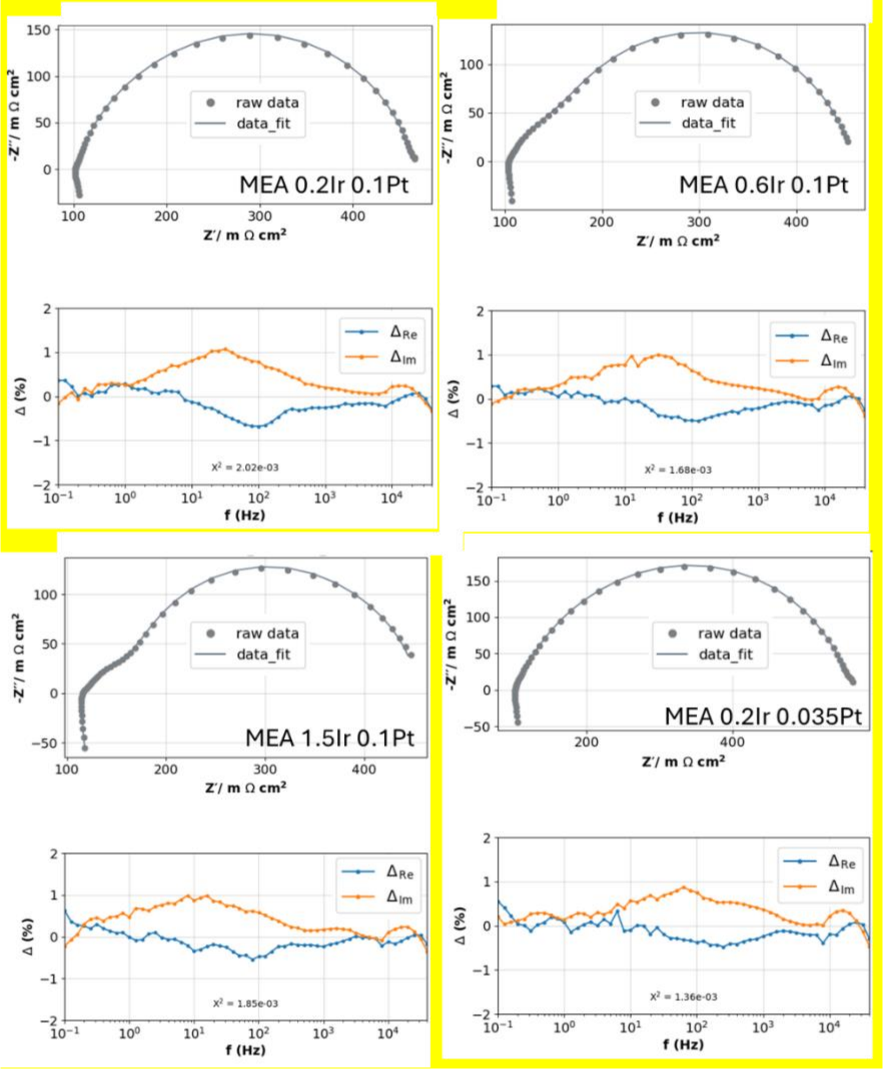

Table S 5. Parameters obtained during DRT algorithms by varying λ_{PG}.

MEA	Varied λ_{PG}	1e-06	1e-05	1e-04	1e-03	1e-02	1e-01
1.5Ir0.1Pt	R_{pol} (mΩcm^2)	320	320	320	320	320	320
	Fitted λ_T, initial λ_T=1e-13	1.00e-12	1.00e-12	6.41e-14	3.75e-13	9.68e-13	2.78e-13
	Fitted λ_{PG}	1.00e-5	1.78e-5	1.06e-4	9.12e-3	1.12e-2	5.80e-2
	Initial Tikhonov residual	8.86e-13	8.86e-13	8.86e-13	8.86e-13	8.86e-13	8.86e-13
	Final Tikhonov residual	1.35	1.35	0.05	1.84e-4	1.51e-4	14.72
0.2Ir0.035Pt	R_{pol} (mΩcm^2)	461	461	461	461	461	461
	Fitted λ_T, initial λ_T=1e-14	9.41e-14	5.78e-14	7.71e-14	5.39e-14	3.94e-14	1.76e-14
	λ_{PG}	8.64e-6	2.62e-5	2.00e-4	2.00e-3	9.98e-3	3.65e-2
	Initial Tikhonov residual	6.60e-13	6.60e-13	6.60e-13	6.60e-13	6.60e-13	6.60e-13
	Final Tikhonov residual	1.87	0.73	9.39e-3	9.50e-4	9.16e-4	5.25e-5
0.6Ir0.1Pt	R_{pol} (mΩcm^2)	349	349	349	349	349	349
	Fitted λ_T, initial λ_T=1e-13	9.68e-13	4.96e-13	6.48e-13	8.56e-13	5.05e-13	2.80e-13
	λ_{PG}	8.49e-6	1.57e-5	1.00e-4	5.20e-3	1.00e-2	5.82e-2
	Initial Tikhonov residual	6.92e-13	6.92e-13	6.92e-13	6.92e-13	6.92e-13	6.92e-13

	Final Tikhonov residual	1.80	0.98	5.58e-2	1.15e-4	1.05e-4	16.3
0.2Ir0.1Pt	R_{pol} (mΩcm^2)	365	365	365	365	365	365
	Fitted λ_T, initial λ_T=1e-9	1.00e-8	5.06e-9	8.59e-10	7.85e-10	6.14e-10	1.00e-10
	Fitted λ_{PG}	5.23e-6	2.02e-5	9.74e-4	3.24e-3	1.00e-2	4.25e-2
	Initial Tikhonov residual	3.13e-13	3.13e-13	3.13e-13	3.13e-13	3.13e-13	3.13e-13
	Final Tikhonov residual	6.85e-1	1.42e-1	1.70e-4	5.49e-5	5.84e-5	5.52e-5

Table S 6. Parameters obtained during DRT algorithms by varying λ_T. λ_{PG}=1e-02.

MEA	Varied λ_T	1e-10	1e-11	1e-12	1e-13	1e-14	1e-15
1.5Ir0.1Pt	R_{pol} (mΩcm^2)	320	320	320	320	320	320
	Fitted λ_T	1.10e-10	5.05e-11	5.05e-12	9.68e-13	3.94e-14	6.20e-15
	Fitted λ_{PG}, initial λ_{PG}=1e-02	1.00e-2	1.00e-2	1.00e-2	1.11e-2	9.95e-3	9.13e-3
	Initial Tikhonov residual	3.186e-13	3.36e-13	4.22e-13	8.86e-13	9.37e-13	9.40e-13
	Final Tikhonov residual	1.65e-4	1.36e-4	2.16e-4	1.51e-4	2.82e-4	3.36e-4
0.2Ir0.035Pt	R_{pol} (mΩcm^2)	461	461	461	461	461	461
	Fitted λ_T	7,87e-11	1.57e-11	5.75e-13	1.59e-13	1.76e-14	5.05e-15
	Fitted λ_{PG}, initial λ_{PG}=1e-01	4.03e-2	3.64e-2	4.15e-2	3.68e-2	3.65e-2	3.64e-2
	Initial Tikhonov residual	3.38e-13	4.20e-13	3.68e-13	5.53e-13	6.50e-13	6.33e-13
	Final Tikhonov residual	5.18e-5	5.25e-5	4.49e-5	5.48e-5	5.25e-5	5.48e-5
0.6Ir0.1Pt	R_{pol} (mΩcm^2)	349	349	349	349	349	349
	λ_T	1.10e-10	5.05e-11	5.05e-12	5.05e-13	5.72e-14	5.24e-15
	Fitted λ_{PG}, initial λ_{PG}=1e-02	1.00e-2	1.00e-2	1.00e-2	1.00e-2	1.60e-2	1.29e-2
	Initial Tikhonov residual	2.39e-13	2.98e-13	3.15e-13	6.92e-13	8.04e-13	8.03e-13
	Final Tikhonov residual	6.74e-5	5.96e-5	6.55e-5	1.05e-4	1.34e-4	1.08e-4

	Varied λ_T	1e-8	1e-9	1e-10	1e-11	1e-12	1e-13
0.2Ir0.1Pt	R_{pol} ($m\Omega cm^2$)	365	365	365	365	365	365
	Fitted λ_T	1.00e-9	7.85e-10	5.99e-10	7.77e-11	7.28e-12	9.95e-13
	Fitted λ_{PG}, initial λ_{PG}=1e-03	6.85e-4	3.24e-3	3.08e-3	3.87e-3	3.88e-3	7.91e-3
	Initial Tikhonov residual	3.52e-13	3.13e-13	3.18e-13	3.53e-13	4.55e-13	9.62e-13
	Final Tikhonov residual	2.63e-3	5.49e-5	6.04e-5	6.80e-5	8.36e-5	1.50e-4

Table S 7. Thickness of anode (An) and cathode (Ca) from SEM measurement

MEA (An/Ca)	Thickness from spot 1-4	Average values
0.2Ir 0.1Pt (An Pristine)	2.85, 2.82, 2.58, 2.86	2.78±0.30
0.2Ir 0.1Pt (An EOL)	4.66, 5.06, 4.27, 4.76	4.69±0.64
0.2Ir 0.035Pt (Ca EOL)	1.67, 1.94, 1.75, 1.91	1.82±0.71
1.5Ir 0.1Pt (An Pristine)	12.2, 12.1, 11.4, 12.3	12.0±0.60
1.5Ir 0.1Pt (An EOL)	13.6, 12.7, 12.0, 13.6	13.0±2.02
1.5Ir 0.1Pt (Ca EOL)	4.66, 3.87, 3.18, 3.67	3.85±1.06